Fission probabilities of ^{242}Am,^{243}Cm, and ^{244}Cm induced by transfer reactions

G. Kessedjian, B. Jurado, G. Barreau, P. Marini, L. Mathieu, I. Tsekhanovich, M. Aiche, G. Boutoux, S. Czajkowski, and Q. Ducasse

Phys. Rev. C **91**, 044607 — Published 9 April 2015

DOI: 10.1103/PhysRevC.91.044607

Fission probabilities of ^{242}Am, ^{243}Cm and ^{244}Cm induced by transfer reactions

G. Kessedjian[a,b,1], *B. Jurado*[a,2], *G. Barreau*[a], *P. Marini*[a], *L. Mathieu*[a],
I. Tsekhanovich[a], *M. Aiche*[a], *G. Boutoux*[a,3], *S. Czajkowski*[a], *Q. Ducasse*[a]

[a] CENBG, Université de Bordeaux, CNRS/IN2P3, Chemin du Solarium, B.P. 120, 33175 Gradignan, France

[b] LPSC, Université Grenoble-Alpes, CNRS/IN2P3, 53 rue des Martyrs, 38026 Grenoble Cedex, France

Abstract :
We have measured the fission probabilities of ^{242}Am, ^{243}Cm and ^{244}Cm induced by the transfer reactions ^{243}Am(^{3}He,^{4}He), ^{243}Am(^{3}He,t) and ^{243}Am(^{3}He,d), respectively. The details of the experimental procedure and a rigorous uncertainty analysis, including a correlation matrix, are presented. For ^{243}Cm our data show clear structures well below the fission threshold. To our knowledge, it is the first time that these structures have been observed for this nucleus. We have compared the measured fission probabilities to calculations based on the statistical model, to obtain information on the fission barriers of the produced fissioning nuclei.

PACs: 25.85.Ge; 25.55.Hp; 24.60.Dr

1. Introduction

Fission probabilities are highly sensitive to fission-barrier properties and level densities at different deformations, and provide valuable information on these fundamental nuclear quantities. Transfer reactions with light projectiles have often been used in the past to induce fission, see e.g. [1-6]. The fission probabilities obtained in these measurements were frequently used to investigate the fission thresholds below the neutron separation energy (S_n) of even-even fissioning nuclei, which are not accessible in neutron-induced reactions, e.g. [7]. These studies were crucial for understanding the origin of the sub-barrier resonances observed in the fission probabilities [8]. These resonances arise from the coupling of the compound nuclear states in the first well to collective vibrations in the fission degree of freedom in the second potential well. The comparison of experimental fission probabilities with statistical model calculations [9] provided also indirect but compelling evidence that the first fission barrier is axially asymmetric for most of the actinide region, as predicted by theoretical calculations of the potential energy surface [10]. In addition, measurements of fission probabilities combined with fission-fragment angular distributions yield information on the

---

[1] kessedjian@lpsc.in2p3.fr

[2] jurado@cenbg.in2p3.fr

[3] Present address: CELIA, 351 Cours de la libération, F-33405 Talence cedex

properties of the transition states at the two saddle points through which the nucleus may pass on its way to fission [11-14].

Another important advantage of transfer-induced fission is that it may enable the formation of very short-lived fissionable nuclei that cannot be produced in neutron-induced reactions because of the high radioactivity of the required targets. Britt and Cramer observed that fission probabilities obtained in transfer reactions were similar to fission probabilities deduced from neutron-induced measurements [15]. This lead to the development of the surrogate-reaction method [16], an indirect technique to infer neutron-induced cross sections for unstable nuclei. In most applications of the surrogate method, the neutron-induced cross section is obtained by multiplying the measured decay probability with the calculated cross section for the formation of a compound nucleus via neutron absorption. This technique has recently received renewed attention and considerable effort has been made from both the experimental and theoretical sides to establish to which extent the surrogate method can be used to infer neutron-induced cross sections [17]. The spin J and parity π distributions populated in the neutron-induced and surrogate reactions can be very different. The impact of this spin-parity mismatch on the different types of cross sections that can be obtained with the surrogate-reaction method is an important subject that requires further experimental and theoretical investigations.

In ref. [18] we used the ^{243}Am(^{3}He,^{4}Hef)^{242}Am, ^{243}Am(^{3}He,tf)^{243}Cm and ^{243}Am(^{3}He,df)^{244}Cm transfer reactions as surrogate reactions for the ^{241}Am(n,f), ^{242}Cm(n,f) and ^{243}Cm(n,f) reactions, respectively. Our results are in very good agreement with the neutron-induced data, even at relatively low excitation energy. In the present work we give the details of the experimental setup and the data analysis procedure employed to derive the fission probabilities used in ref. [18]. The transfer reactions considered here have already been studied by Gavron et al. [9]. However, our measurements cover a broader range of excitation energies and we have carried out a thorough uncertainty analysis of the fission probabilities, paying special attention to parameter correlations and their effect on the final data uncertainties. In the last part of this work we compare our results to simplified statistical-model calculations to extract fission barrier parameters.

2. Experiment and data analysis

When fission of a nucleus A is induced by a transfer reaction $X(y,b)A$, the fission probability P_f as a function of excitation energy E^* can be obtained as:

$$P_f^A(E^*) = \frac{N_{coinc}^b(E^*)}{N_{sing}^b(E^*) \cdot \varepsilon_f(E^*)} \tag{1}$$

where N_{sing}^b is the total number of detected ejectiles b, N_{coinc}^b is the number of ejectiles b detected in coincidence with a fission fragment and ε_f is the fission-detection efficiency. In the absence of parasitic transfer reactions with the same ejectile b, the quantity $N_{coinc}^b / \varepsilon_f$

gives the number of compound nuclei A that have undergone fission amongst the number of formed compound nuclei N^{b}_{sing}.

In a recent work [19], where fission was induced via multinucleon transfer between ^{12}C and ^{238}U, a non negligible probability of exciting the carbon-like ejectiles was observed, that questioned the commonly used assumption that the excitation energy available in the transfer reaction is found only in the heavy reaction partner. In this work, we deal with ^{3}He-induced transfer reactions where the ejectile can be a deuteron, a triton or an α particle, and the maximum total available excitation energy is essentially below 20 MeV. Deuterons and tritons have no bound excited states and will break up if excited, while the first excited state of ^{4}He is located at 20.2 MeV. Therefore, all the *detected* ejectiles are in their ground state and all the excitation energy available in the reaction can safely be attributed to the fissioning nucleus A. The excitation energy can then be unambiguously determined from the measured kinetic energy E_b and emission angle θ of the ejectile, by applying energy and momentum conservation laws:

$$E^* = \frac{M_A Q - E_y(M_y - M_A) - E_b(M_A + M_b) + 2\sqrt{M_y M_b E_y E_b}\cos\theta}{M_A} \tag{2}$$

where the different M_i represent the masses of the nuclei involved in the reaction, Q is the Q-value of the transfer reaction and E_y is the beam energy. Tritons and ^{3}He break up at excitation energies of 6.2 and 5.5 MeV, respectively. In principle, the deuterons that result from the breakup may pollute the (^{3}He,d) reaction. However, in the work by Gavron et al. [9] the fission probabilities of various nuclei formed both via (^{3}He,d) and (^{3}He,t) reactions were compared and found to be in good agreement, thus demonstrating that contamination due to ^{3}He or triton breakup can be disregarded. For these measurements, Gavron et al. used a beam energy of 25 MeV and a particle telescope placed at 120 degrees. Therefore, to avoid the possible background generated by ^{3}He or triton breakup we have used in our measurement experimental conditions similar to Gavron et al.

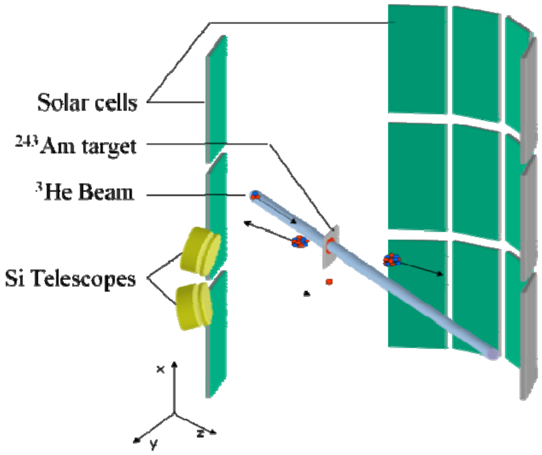

Figure 1: (Color online) Schematic three-dimensional representation of the set-up for fission probability measurements.

The measurement was conducted at the Tandem accelerator of the IPN Orsay that delivered a ^{3}He beam of 24 MeV with an intensity of about 50 nAe. The ^{243}Am ($T_{1/2}$=7370 y) target, of approximately 150 µg/cm^2 thickness, 99.85% (±0.01%) isotopic purity and 6 mm diameter, was prepared by electrodeposition by the Argonne National Laboratory. The ^{243}Am layer was deposited on a 75 µg/cm^2 natural carbon backing. The set-up used to determine the fission probabilities is shown in Fig. 1. Ejectiles were detected by two telescopes placed at 5 cm from the target and centered at 130^o with respect to the beam axis. The telescopes had an aperture of 7 mm diameter leading to an angular uncertainty $\Delta\theta$ of ±4^o. The energy-loss ΔE was measured with a 150 µm thick Si detector and the residual energy E with a Si-Li detector of 5 mm thickness. An Al foil of 29 µm was placed in front of the telescopes to stop fission fragments and α particles coming from the activity of the ^{243}Am target. Fission fragments were detected in coincidence with the ejectiles with a fission-fragment multi-detector, consisting of 15 photovoltaic cells arranged in 5 units in a cylindrical geometry. Each unit was composed of 3 cells placed in a vertical row. For each unit, the center of the middle cell was in the horizontal reaction plane defined by the beam. Four units were located in forward direction covering an angular range from 14^o to 125^o. The fifth unit was positioned at 180^o from the foremost unit. Each cell had an active area of 19.8 x 40.2 mm^2. The radius of the cylinder supporting the cells was 5 cm. The beam was stopped in a Faraday cup connected to an integrator to measure the deposited charge. The amplified signals of the telescopes and the fission detectors were digitized with an ADC. All the detector signals were pulse-shaped into fast timing signals and sent to a TDC to measure the time differences between the telescopes and the fission detectors. The acquisition system was triggered by the ΔE-E coincidences of either one or the other telescope.

Reaction	Q-Value (MeV)	E* of excited states (MeV)	Energy of ejectiles emitted at 130° (MeV)
^{208}Pb(^{3}He,d)^{209}Bi*	-1.696	0	21.41
		0.896	20.53
		1.608	19.83
		2.826	18.63
		3.119	18.34
		3.633	17.83
^{208}Pb(^{3}He,^{4}He)^{207}Pb*	+13.21	0	35.54
		0.570	34.98
		0.898	34.66
		1.633	33.95
		2.340	33.26
		3.476	32.16

Table 1: Kinetic energies of the ejectiles corresponding to the excited states of ^{209}Bi and ^{207}Pb used for the energy calibration of the telescopes.

2.1. Energy calibration

Because of the rapid increase of the fission probability with excitation energy at the fission threshold, it is extremely important to accurately calibrate in energy the particle telescopes. In this work we consider kinetic energies ranging from 5 to 25 MeV for deuterons and tritons and from 17 to 37 MeV for alphas. Thus, the kinetic energies can be much higher than the kinetic energies of the alpha particles originating from a standard calibration source. Moreover, it is well known that the response of Si detectors to hydrogen isotopes differs from the response to alphas of the same kinetic energy [20]. For these reasons, in this work the telescopes were calibrated with known energy lines from chosen reactions on a lead target. We used a ^{208}Pb target of 200 μg/cm^2 and a ^{3}He beam of 24 MeV to populate the first excited states of ^{209}Bi and ^{207}Pb via the transfer reactions ^{208}Pb(^{3}He,d) and ^{208}Pb(^{3}He,^{4}He), respectively. For the energy calibration, the aperture of the Si telescopes was reduced to 2 mm to limit the kinematic spread. The telescopes provided the identification of the ejectiles as well as their scattering angles. This information, the Q-values of the transfer reactions used and the *E** of the first excited states of ^{209}Bi and ^{207}Pb (which are known with high accuracy) were used to calculate the kinetic energy of the corresponding ejectiles. In this way we had a source of deuterons and alphas with very well defined kinetic energies in the range of interest for the present work. The excitation energy of the states considered for the calibration and the associated kinetic energies of the ejectiles detected at 130° are reported in Table 1. A conventional identification plot representing the energy loss vs. the residual energy in the telescope obtained after the interaction of a ^{3}He beam on ^{208}Pb is shown in Fig. 2. The lines correspond to different ejectiles and indicate the formation of a specific nucleus. The ground state and the first excited states of ^{209}Bi and ^{207}Pb can be clearly distinguished. The calibration coefficients obtained with the ^{208}Pb(^{3}He,d) reaction were used in the analysis of the ^{243}Am(^{3}He,d) and the ^{243}Am(^{3}He,t) reactions.

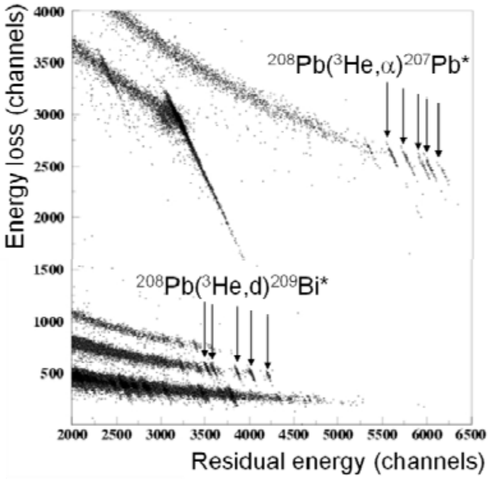

Fig. 2: Energy loss versus residual energy as measured in one of the Si telescopes for the ^{3}He + ^{208}Pb reaction at 24 MeV beam energy. The ground state and first excited states of ^{209}Bi and ^{207}Pb are indicated by arrows.

2.2. Singles and coincidence spectra

Fig. 3 shows the identification plot for the ^{3}He + ^{243}Am reaction at 24 MeV. By selecting one type (*Z*, *A*) of ejectile, for example ^{4}He, the so-called "singles" spectrum $N_{sing}(E^*)$, can be obtained. In this particular case, it represents the number of detected ^{242}Am nuclei as a function of their excitation energy.

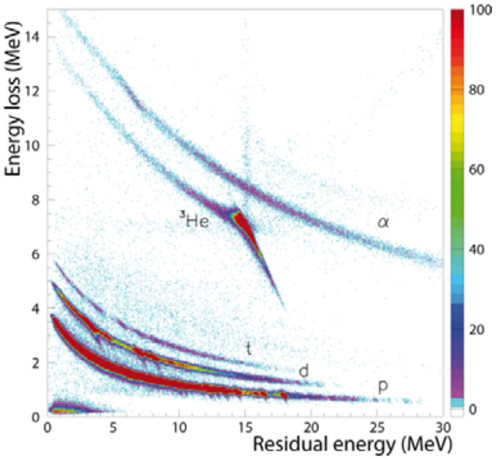

Fig. 3: (Color online) Energy loss versus residual energy in one of the Si telescopes for the ^{3}He + ^{243}Am reaction at 24 MeV. The ejectiles associated to the different Z lines are indicated.

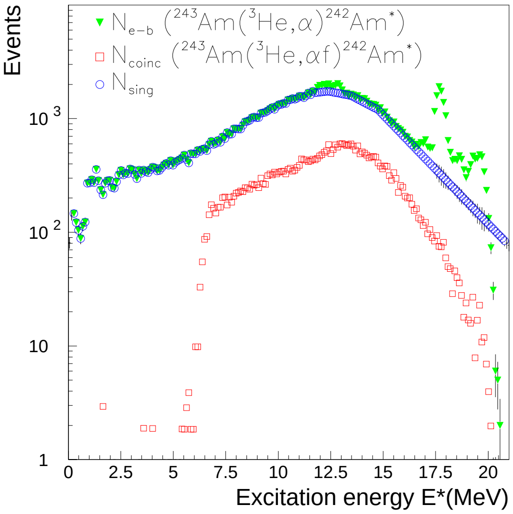

Fig. 4: (Color online) Number of detected ^{4}He (green triangles) ejectiles as a function of the excitation energy of ^{242}Am after subtraction of events coming from reactions on the target backing. The ^{4}He ejectiles stemming from reactions on target contaminants are present above 12 MeV. The blue circles represent the singles spectrum $N_{sing}(E^*)$ after interpolation and the red squares the fission coincidence spectrum $N_{coin}(E^*)$ for ^{242}Am (see text).

The singles spectrum is derived from the spectrum of ^{4}He as a function of the excitation energy of ^{242}Am represented by the triangles on Fig. 4. The broad peaks at the highest excitation energies in the ^{4}He spectrum stem from transfer reactions on the ^{13}C present in the carbon backing and on ^{16}O, ^{19}F and ^{35,37}Cl impurities in the target. The background from reactions on the carbon support was measured separately with a carbon target with the same characteristics as the target backing. It was subtracted from the singles spectrum after being properly normalized. The normalization factor was given by the ratio between the integrated beam intensities measured for the ^{243}Am target and the separated C backing. In the excitation-energy range considered here, the only contribution to the ^{4}He spectrum due to the carbon backing comes from the interaction of the beam with ^{13}C, which is present in a very small amount in the natural carbon backing. The spectrum resulting from the subtraction of these events is labeled as $N_{e\text{-}b}$ in Fig. 4, and in this case is basically equivalent to the ^{4}He spectrum before subtraction. The singles spectrum N_{sing} was obtained by interpolating the $N_{e\text{-}b}$ spectrum under the remaining contaminant peaks (see circles in Fig. 4). This introduces an additional source of uncertainty that will be discussed in section 3.

Fig. 5 shows the energy spectrum of fission fragments detected in coincidence with deuterons. The double-humped structure due to the different kinetic energies of the light and heavy fission fragments can be clearly distinguished. This spectrum was generated without applying any condition on the time difference between the telescope and the relevant solar cell. Still, the spectrum is not polluted by random coincidences with the alpha particles originating from the activity of the ^{243}Am target.

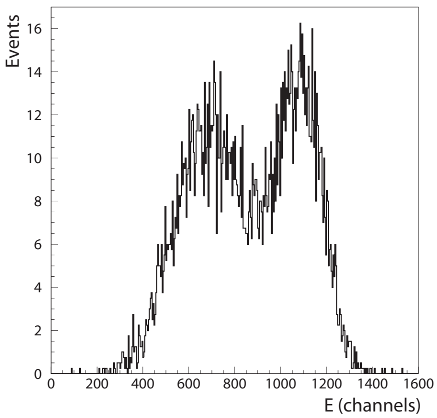

Fig. 5: Energy spectrum of fission fragments detected in one solar cell in coincidence with deuterons detected in one telescope.

Ejectile-fission coincidences, $N_{coinc}(E^*)$, were determined by selecting those events for which the time difference between the telescope and the solar-cells signals was within a chosen coincidence window. The time spectra for the deuteron, triton and alpha-transfer channels and the applied time selections are shown in Fig. 6. The width and the double-humped structure of the coincidence peak reflect the time needed by the fragments to reach the fission detector plus the time to collect the charges produced at different positions in the photovoltaic cell. The number of random coincidences present in the time coincidence window is given by the integral of the dashed area shown in the upper panel of Fig. 6. This number was evaluated by determining the number of the random events per channel in the regions of the time spectrum outside the time selection. As seen from Fig. 6, the effect of random coincidences becomes noticeable only for the deuteron channel, however still remaining below 1% of the total number of coincidences. The coincidence spectrum $N_{coinc}(E^*)$ representing the number of detected ^{242}Am nuclei which undergo fission is presented in Fig. 4 as empty squares. This spectrum has been corrected for random coincidences.

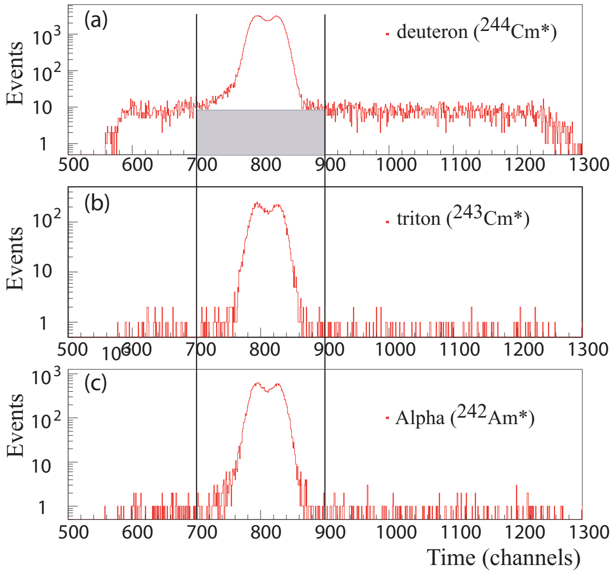

Fig. 6: (Color online) Time difference between one telescope and all the solar cells of the fission detector for the deuteron (a), triton (b) and ^{4}He (c) transfer channels. The vertical lines indicate the selection of coincidence events. The shaded area represents the random coincidences included in this selection.

2.3. Fission-detection efficiency

As indicated in eq. (1), to calculate the fission probability the ratio between the N_{coinc} and N_{sing} spectra needs to be corrected for the fission-detector efficiency $\varepsilon_f(E^*)$. The fission efficiency is given by the solid angle covered by the fission detector (the so-called geometrical efficiency) and the fission-fragment angular anisotropy. The fission-fragment angular anisotropy depends both on the angular momentum of the fissioning nucleus, and on the kinematic focussing due to the recoil energy of the fissioning nucleus. We developed a Monte-Carlo simulation to determine the fission-detection efficiency. The geometrical part of the simulation was validated by measuring the solid angle of our detector with a ^{252}Cf source of known activity. The simulation gives a geometrical efficiency of (45.2 ± 1.5)%. The uncertainty is dominated by the uncertainties in the detector geometry. The segmentation of our fission detector in 15 cells, located at different positions, allowed us to measure the angular distribution of the fission fragments as a function of E^*. To cumulate enough statistics the excitation-energy bin was chosen 210 keV wide. The left part of Fig. 7 shows an example of fission-fragment angular distribution for ^{243}Cm at E^*=7.5 MeV. The data were fitted with the function:

$$W(\theta_{cm}) = \frac{dN}{d\Omega}(\theta_{cm}) = a \cdot \cos^2(\theta_{cm}) + b \tag{3}$$

where θ_{cm} is the emission angle of the fission fragment in the centre of mass of the fissioning nucleus.

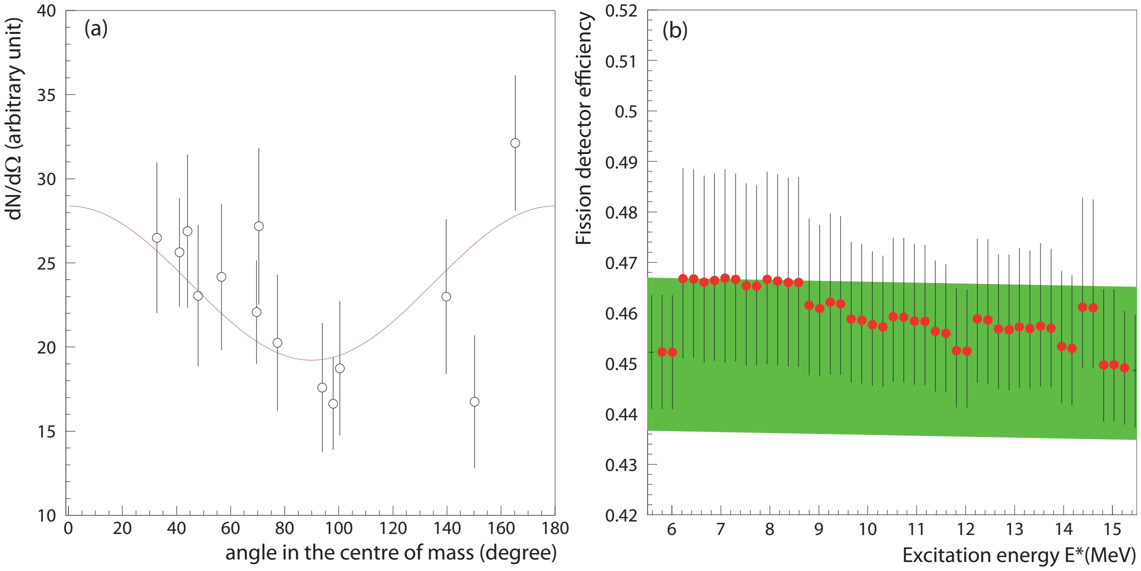

Fig. 7: (Color online) (a) Angular distribution of fission fragments for ^{243}Cm at E^*=7.5 MeV. The number of detected fission events divided by the solid angle subtended by the corresponding cell is shown as a function of the average emission angle of the fragments in the centre of mass of the fissioning nucleus. The full line represents the fit function according to eq. (3) with $\frac{W(0°)}{W(90°)} = 1 + \frac{a}{b} = 1.47 \pm 0.17$ and reduced chi-squared χ^2=0.96**.** (b) Fission-detector efficiency as a function of E^* of ^{243}Cm. The shaded area corresponds to the geometrical efficiency of our fission detector including the corresponding uncertainty. The symbols represent the effective fission efficiency including the fission-fragment angular anisotropy and kinematic effects caused by the recoil energy of ^{243}Cm.

The effective efficiency for each E^* bin was calculated with the Monte-Carlo simulation including the experimental angular anisotropies in the centre of mass and kinematical effects. The right panel of Fig. 7 shows the effective efficiency as a function of excitation energy compared to the geometrical efficiency. Because of the high geometrical efficiency of our detector, the corrections on the final detector efficiency due to the fission-fragment angular anisotropy amount to 2-3 % at most and do not exceed the error due to the uncertainty in the geometry of the detector. Therefore, the uncertainty of the effective efficiency is dominated by the uncertainty in the detector geometry. We observed this low sensitivity to the angular anisotropy in all the reactions studied. For this reason, hereafter we consider that the effective efficiency is equal to the efficiency including kinematical effects and that the uncertainty in the effective efficiency is equal to the uncertainty in the detector geometry for all the reactions.

3. Uncertainty analysis

In this section we discuss how the uncertainties and the correlation matrix for the uncertainties of the measured data were obtained. The accurate determination of the uncertainties requires very detailed information on the experimental procedure that is best known by the experimentalists who performed the measurements. In the first part of this section we will show that the variance of the measured probabilities can be strongly affected by the correlation between some of the quantities involved in the determination of the fission probability. Moreover, in this experiment the probabilities were measured at different energies with the same set-up. Thus, they are not completely independent, and the covariance between the fission probabilities at different energies should be determined. This will be discussed in the second part of this section. When data at different energies are partially correlated, there is a degree of “stiffness”, implying that the data at a given energy cannot be modified independently from the data at the other energies. The covariance matrix of experimental data represents a key piece of information for providing the evaluated covariance matrix [21], which can have a strong impact in applications like e.g. the simulation of critical assemblies.

3.1. Variance of the fission probability measurements

Because in this experiment we have used two telescopes, we have adopted an explicit notation for the l^{th} fission probability P_f of nucleus A measured with the l^{th} silicon telescope at energy E_i^*:

$$P_f^{l,A}(E_i^*) = P_i^l = \frac{N_{coinc,i}^l}{N_{sing,i}^l \cdot \varepsilon_{f,i}} \tag{4}$$

The relative uncertainty on the fission probability is given by:

$$\begin{aligned}\frac{Var(P_i^l)}{\left(P_i^l\right)^2} = \frac{Var(N_{coinc,i}^l)}{\left(N_{coinc,i}^i\right)^2} + \frac{Var(N_{\text{sing,i}}^l)}{\left(N_{\text{sing,i}}^l\right)^2} + \frac{Var(\varepsilon_{f,i})}{\left(\varepsilon_{fi}\right)^2} - 2 \cdot \frac{Cov(N_{coinc,i}^l; N_{\text{sing,i}}^l)}{N_{coinc,i}^l \cdot N_{\text{sing,i}}^l} \\ - 2 \cdot \frac{Cov(N_{coinc,i}^l; \varepsilon_{f,i})}{N_{coinc,i}^l \cdot \varepsilon_{f,i}} + 2 \cdot \frac{Cov(N_{\text{sing,i}}^l; \varepsilon_{f,i})}{N_{\text{sing,i}}^l \cdot \varepsilon_{f,i}}\end{aligned} \tag{5}$$

where *Var* is the variance and *Cov* the covariance. As mentioned in section 2.3, the geometrical fission-fragment efficiency $\varepsilon_{f,i}$ was determined with a ^{252}Cf source. Different supports were used for the source and the ^{243}Am target. Therefore, in this experiment the efficiency measurement was completely independent of the measurement of $N_{coinc,i}^l$ and $N_{\text{sing},i}^l$ and the two last covariance terms in eq. (5) can be disregarded.

To assess the first covariance term $Cov(N_{coinc,i}^l; N_{sing,i}^l)$, we consider the number of singles events as the union of two elementary sets: the fission-fragment−ejectile coincidence set, associated to the random variable $N_{coinc,i}^l$, and the set of ejectiles in anticoincidence with a fission fragment associated to the random variable $N_{acoinc,i}^l$. It follows that:

$$N_{sing,i}^l = N_{coinc,i}^l + N_{acoinc,i}^l \tag{6}$$

Because in this experiment the solid angle of the particle telescopes was rather small, less than 1%, using eq. (6), fluctuations in N_{coinc} will generally have no impact on N_{acoinc} (and vice versa), and $Cov(N_{coinc};N_{acoinc})$ can be disregarded. Consequently, we have:

$$\begin{aligned}
&Cov(N^{l}_{coinc,i};N^{l}_{sing,i}) = Cov(N^{l}_{coinc,i};N^{l}_{acoinc,i}) + Var(N^{l}_{coinc,i}) \qquad \forall\, l, \forall\, i \\
&and\; Cov(N^{l}_{coinc,i};N^{l}_{acoinc,i}) \approx 0 \qquad \forall\, l, \forall\, i \\
&then\; Cov(N^{l}_{coinc,i};N^{l}_{sing,i}) \approx Var(N^{l}_{coinc,i}) \qquad \forall\, l, \forall\, i
\end{aligned} \tag{7}$$

The linear interdependence between $N^{l}_{coinc,i}$ and $N^{l}_{sing,i}$ can be quantified with the correlation coefficient *Corr,* defined as the ratio of the covariance over the product of the standard deviations. This dimensionless quantity takes values within the interval [-1;1]:

E^{*} (MeV)	$N^{1}_{sing,i}$	$\frac{\sqrt{Var(N^{1}_{sing,i})}}{N^{1}_{sing,i}}$ (%)	$N^{1}_{coinc,i}$	$\frac{\sqrt{Var(N^{1}_{coinc,i})}}{N^{1}_{coinc,i}}$ (%)	$Corr(N^{1}_{coinc,i};N^{1}_{sing,i})$	P^{1}_{i}	$\left.\frac{\sqrt{Var(P^{1}_{i})}}{P^{1}_{i}}\right\|_{stat}$ without $Corr(N^{1}_{coinc,i};N^{1}_{sing,i})$ (%)	$\left.\frac{\sqrt{Var(P^{1}_{i})}}{P^{1}_{i}}\right\|_{stat}$ with $Corr(N^{1}_{coinc,i};N^{1}_{sing,i})$ (%)
9.66	2464	2.01	645	3.94	0.51	0.58	4.42	3.38
12.45	3459	1.70	1083	3.10	0.56	0.69	3.48	2.52
14.60	2480	2.00	922	3.12	0.61	0.82	3.85	2.61

Table 2: Relative statistical uncertainty of the fission probability with and without inclusion of the correlation between $N^{l}_{coinc,i}$ and $N^{l}_{sing,i}$. The uncertainty in the 8th column includes only the two first terms of eq. (5) and the one in the 9th column includes the first two terms and the fourth term of eq. (5). The data correspond to the ^{243}Am(^{3}He,^{4}He) reaction and telescope 1.

Table 2 shows three examples that illustrate the influence of the term $Cov\left(N^{l}_{coinc,i};N^{l}_{sing,i}\right)$ on the relative statistical uncertainty on the fission probability. In the third and fourth lines the statistical relative uncertainty of the fission probability without inclusion of the covariance between $N^{l}_{coinc,i}$ and $N^{l}_{sing,i}$ is over estimated by more than 30%. One can also notice that the correlation between $N^{l}_{coinc,i}$ and $N^{l}_{sing,i}$ increases with the square root of the fission probability.

In the following, our goal is to assess the systematic uncertainties on $N^{l}_{sing,i}$ associated to the contaminant corrections. As mentioned in section 2.2, $N^{l}_{sing,i}$ is obtained by subtracting from the detected ejectiles $N^{l}_{\mathrm{eje,i}}$ the background generated by the ejectiles originating from transfer reactions on the C-backing $N^{l}_{back,i}$ and on target contaminants $N^{l}_{cont,i}$:

$$N^{l}_{\sin g,i} = N^{l}_{eje,i} - N^{l}_{back,i} - N^{l}_{cont,i} \tag{8}$$

To simplify the notation we introduce the quantity $N^l_{\text{e-b,i}}$, representing the number of ejectiles after subtraction of the contribution of the target-backing:

$$N^l_{e\text{-}b,i} = N^l_{eje,i} - N^l_{back,i} \tag{9}$$

$N^l_{eje,i}$ and $N^l_{back,i}$ are uncorrelated because these two quantities were obtained in two separated measurements, and thus $Cov(N^l_{eje,i};N^l_{\text{back,i}}) = 0$ for all energies E^*_i. Therefore, the uncertainty of $N^l_{\text{e-b,i}}$ is:

$$Var\left(N^l_{e\text{-}b,i}\right) = Var\left(N^l_{eje,i}\right) + Var\left(N^l_{back,i}\right) \tag{10}$$

The contaminant peaks are located at relatively high excitation energies, where the level density of the actinides investigated is very high and the corresponding singles spectrum should vary smoothly with E^*. For this reason, we have assumed that the singles spectrum at the positions of the contaminant peaks is given by a smooth function exp(aE^*+b), where the constants a and b are such that the singles spectrum is equal to $N^l_{e-b,i}$ right before and after the contaminant peak. The $N^l_{\text{sing,i}}$ spectrum results from the union of the $N^l_{e-b,i}$ spectrum before the contaminant peak and the smooth exponential function below the contaminant peak, see Fig. 4.

From eq. (8) and eq. (9) we get the number of contaminant reactions $N^l_{cont,i}$ as a function of the assumed singles spectrum $N^l_{\text{sing,i}}$:

$$\begin{aligned} N^l_{cont,i} &= N^l_{\text{e-b,i}} - N^l_{\text{sing,i}} \\ Var\left(N^l_{cont,i}\right) &= Var\left(N^l_{\text{e-b,i}}\right) + Var\left(N^l_{\text{sing,i}}\right)_{stat} - 2\cdot Cov\left(N^l_{\text{e-b,i}};N^l_{\text{sing,i}}\right) \end{aligned} \tag{11}$$

where $Var\left(N^l_{\text{sing,i}}\right)_{stat} = N^l_{\text{sing,i}}$ is the statistical variance of the number of assumed single events.

In order to account for the strong interdependence between the singles and the contaminant spectra in this analysis, we assume a full correlation between $N^l_{\text{e-b,i}}$ and $N^l_{\text{sing,i}}$:

$$Cov(N^l_{e-b,i};N^l_{\text{sing},i}) = \sqrt{Var\left(N^l_{e\text{-}b,i}\right)\cdot Var\left(N^l_{\text{sing},i}\right)_{stat}} \tag{12}$$

Using eqs. (8), (11) and (12) it follows that:

$$\begin{aligned} Var\left(N^l_{\sin g,i}\right)_{total} &= Var\left(N^l_{e\text{-}b,i}\right) + Var\left(N^l_{cont,i}\right) \\ Var\left(N^l_{\sin g,i}\right)_{total} &= Var\left(N^l_{\text{sing},i}\right)_{stat} + 2\cdot\sqrt{Var\left(N^l_{e\text{-}b,i}\right)}\cdot\left(\sqrt{Var\left(N^l_{e\text{-}b,i}\right)} - \sqrt{Var\left(N^l_{\text{sing},i}\right)_{stat}}\right) \end{aligned} \tag{13}$$

The covariance term between $N^l_{\text{e-b,i}}$ and $N^l_{cont,i}$ is included in the variance of $N^l_{cont,i}$. The first term of the second eq. (13) corresponds to the statistical uncertainty and the second one to the systematic uncertainty. We observe that the systematic uncertainty is zero if there is no contribution to the spectrum from the contaminants and it is positive if there are contaminants. The quantification of the systematic uncertainty in $N^l_{\text{sing,i}}$ is needed to define the covariance matrix of the fission-probability measurements at different excitation energies (see section 3.2).

The corrections due to the target-backing and the contaminants were determined independently for each telescope. Therefore, the statistical and systematic variances for the l^{th} fission-probability measurement are defined by the following equations:

$$\begin{gathered}\frac{Var\left(P_i^l\right)_{stat}}{\left(P_i^l\right)^2}=\frac{Var\left(N^l_{coinc,i}\right)}{\left(N^l_{coinc,i}\right)^2}+\frac{Var\left(N^l_{\text{sing,i}}\right)_{stat}}{\left(N^l_{\text{sing,i}}\right)^2}-2\cdot\frac{Var(N^l_{coinc,i})}{N^l_{coinc,i}\cdot N^l_{\text{sing,i}}}\\ \frac{Var\left(P_i^l\right)_{syst}}{\left(P_i^l\right)^2}=\frac{2\cdot\sqrt{Var\left(N^l_{\text{e-b,i}}\right)}\cdot\left(\sqrt{Var\left(N^l_{\text{e-b,i}}\right)}-\sqrt{Var\left(N^l_{\text{sing,i}}\right)_{stat}}\right)}{\left(N^l_{\text{sing,i}}\right)^2}+\frac{Var\left(\varepsilon_{f,i}\right)}{\left(\varepsilon_{f,i}\right)^2}\end{gathered} \tag{14}$$

The final value for the fission probability at excitation energy E_i^* is obtained from the weighted mean of the fission probabilities P_i^l. In this experiment, the two measurements of the fission probability were simultaneously performed with the same target and the same fission detector. As a consequence, only the fission efficiency $\varepsilon_{f,i}$ is common to both measurements and its uncertainty represents the covariance term between the two measurements P_i^l and $P_i^{l'}$ of the fission probability :

$$\frac{Var\left(P_i^l\right)^{\forall l}_{com.syst}}{\left(P_i^l\right)^2}=\frac{Var\left(\varepsilon_f\right)}{\left(\varepsilon_{f,i}\right)^2} \tag{15}$$

$Var\left(\varepsilon_f\right)$ is the geometrical uncertainty on the fission efficiency where the index i has been omitted because the variance on the efficiency is independent of the excitation energy. Nevertheless, the fission efficiency depends on the excitation energy due to the kinematical corrections, as discussed in section 2.3. Eq. (15) corresponds to the common systematic uncertainty for the probability measurements performed at the same excitation energy with the two different telescopes.

To obtain the mean value $\langle P_i\rangle$, the values of P_i^l are weighted by the uncertainty:

$$w_i^l = \frac{Var\left(N^l_{coinc,i}\right)}{\left(N^l_{coinc,i}\right)^2} + \frac{Var\left(N^l_{\mathrm{sing,i}}\right)_{stat}}{\left(N^l_{\mathrm{sing,i}}\right)^2} - 2\cdot\frac{Var(N^l_{coinc,i})}{N^l_{coinc,i}\cdot N^l_{\mathrm{sing,i}}} + \frac{2\cdot\sqrt{Var\left(N^l_{\mathrm{e\text{-}b,i}}\right)}\cdot\left(\sqrt{Var\left(N^l_{\mathrm{e\text{-}b,i}}\right)}\cdot - \sqrt{Var\left(N^l_{\mathrm{sing,i}}\right)_{stat}}\right)}{\left(N^l_{\mathrm{sing,i}}\right)^2} \tag{16}$$

where we have adopted the notation w_i^l for the weight associated to the P_i^l fission probability measurement. The final uncertainty on mean fission probability, $\langle P_i\rangle$, is given by the sum of the uncertainty of the weighted mean and the uncertainty in the fission efficiency. The latter is added only once because it is the common systematic uncertainty (eq.15) to the *m* telescopes (in our case *m* = 2):

$$\begin{gathered}\langle P_i\rangle = \sum_l^{m=2}\frac{P_i^l}{w_i^l}/\sum_l^{m=2}\frac{1}{w_i^l}\\ \frac{Var(\langle P_i\rangle)}{\langle P_i\rangle^2} = \frac{1}{\sum\limits_l^{m=2}\frac{1}{w_i^l}} + \frac{Var\left(\varepsilon_f\right)}{\left(\varepsilon_{fi}\right)^2}\end{gathered} \tag{17}$$

3.2. Covariance of the fission-probability measurements at different excitation energies

The second part of this section is devoted to the evaluation of the covariance term between two mean fission-probability measurements at excitation energies E_i^* and E_j^*. The generalized perturbation theory [23] allows one to define the covariance term as the sum of the variances and covariances of all the measured quantities a_k (in our case a_k represents N_{sing}, N_{coinc}, etc.) weighted by the sensitivity S_{ik} of the observable $\langle P_i\rangle$ to the quantity a_k:

$$\begin{gathered}\frac{Cov(\langle P_i\rangle;\langle P_j\rangle)}{\langle P_i\rangle\cdot\langle P_j\rangle} = \sum_{k=1}^{p}(S_{ik})^2\cdot\frac{Var(a_k)}{(a_k)^2} + 2\cdot\sum_{k>k'}^{p}(S_{ik})\cdot(S_{jk'})\cdot\frac{Cov(a_{ik};a_{jk'})}{a_{ik}\cdot a_{jk'}}\\ \forall\,\mathrm{i}\;\; S_{ik} = \frac{\partial\langle P_i\rangle}{\partial a_k}\cdot\frac{a_k}{\langle P_i\rangle}\end{gathered} \tag{18}$$

The sum runs over the p quantities needed to determine the mean fission probabilities $\langle P_i\rangle$ and $\langle P_j\rangle$. In ref. [22] we have performed a rigorous analysis to apply eq. (18) to our measurement. In this work, we present only the main results and we refer to [22] for the details on the derivation of the following eqs.

In our experiment, the two telescopes were located at the same angle and at the same distance from the target. Therefore, the fission probabilities and statistical uncertainties obtained with the different telescopes have similar values. As shown in [22], in that case, from eqs. (16-18) it follows that the absolute value of the sensitivity of $\langle P_i \rangle$ to a quantity a_k is constant for all the quantities and for all the l^{th} measurements. That is:

$$|S_{ik}| = \frac{Var\langle P_i \rangle}{\langle P_i \rangle} \cdot \frac{P_i^l}{Var\left(P_i^l\right)_{weight}} \approx 1/m \quad , \forall l \tag{19}$$

	l^{th} measurement at energies E_i^* and E_j^*						l'^{th} measurement at energies E_i^* and E_j^*					
a_k $k \in [1;p]$	$N^{l}_{coinc,i}$	$N^{l}_{\text{sing},i}$	ε^{l}_{fi}	$N^{l}_{coinc,j}$	$N^{l}_{\text{sing},j}$	ε^{l}_{fj}	$N^{l'}_{coinc,i}$	$N^{l'}_{\text{sing},i}$	$\varepsilon^{l'}_{fi}$	$N^{l'}_{coinc,j}$	$N^{l'}_{\text{sing},j}$	$\varepsilon^{l'}_{fj}$
$N^{l}_{coinc,i}$	Var	Cov	0	0	0	0	0	0	0	0	0	0
$N^{l}_{\text{sing},i}$		Var	0	0	Cov	0	0	0	0	0	0	0
ε^{l}_{fi}			Var	0	0	Cov	0	0	Cov	0	0	Cov
$N^{l}_{coinc,j}$				Var	Cov	0	0	0	0	0	0	0
$N^{l}_{\text{sing},j}$					Var	0	0	0	0	0	0	0
ε^{l}_{fj}						Var	0	0	Cov	0	0	Cov
$N^{l'}_{coinc,i}$							Var	Cov	0	0	0	0
$N^{l'}_{\text{sing},i}$								Var	0	0	Cov	0
$\varepsilon^{l'}_{fi}$									Var	0	0	Cov
$N^{l'}_{coinc,j}$										Var	Cov	0
$N^{l'}_{\text{sing},j}$											Var	0
$\varepsilon^{l'}_{fj}$												Var
S_{ik}	$1/m$	$-1/m$	$-1/m$	0	0	0	$1/m$	$-1/m$	$-1/m$	0	0	0
S_{jk}	0	0	0	$1/m$	$-1/m$	$-1/m$	0	0	0	$1/m$	$-1/m$	$-1/m$

Table 3: Representation of the variances and covariances of the parameters related to the l^{th} and l'^{th} measurements of the fission probability at two energies E^*_i and E^*_j. The table serves to visualize the correlated and independent measured quantities. The dashed areas indicate the correlated quantities at two energies E_i^* and E_j^* for each l^{th} measurement and the white zone the correlated quantities for the two telescopes. Only the part above the diagonal is displayed. The two last lines give the sensitivity coefficients S defined in eq. (19).

The covariance term associated to the efficiency is:

$$Cov\left(\varepsilon_{f,i};\varepsilon_{f,j}\right)=Var\left(\varepsilon_{f}\right)\ \ \forall \mathrm{i,j} \tag{20}$$

Using the results of eq. (14), it can be shown that the covariance of the l^{th}-probability measurements at different energies is given by [22]:

$$Cov\left(P_i^l;P_j^l\right)=\sqrt{Var\left(P_i^l\right)_{syst}\cdot Var\left(P_j^l\right)_{syst}} \tag{21}$$

In Table 3, we present a synthetic comparison of the correlations of the a_k quantities involved in the mean fission-probability measurements. The data obtained with each telescope (i.e. the data associated to each l^{th} measurement) are treated independently. Consequently, for the l^{th} measurement, the covariance of two fission probabilities at the energies E_i^* and E_j^* is caused by the systematic corrections of the number of singles $N_{\mathrm{sing,i}}^{l}$ due to target contaminants and the common uncertainty in the fission efficiency. For two different fission-probability measurements P_i^l and $P_j^{l'}$ at the energies E_i^* and E_j^*, only the covariance term on the fission efficiency is present.

Using eqs. (20) and (21), it can be shown [22] that the correlation between the mean values of the fission probabilities at two different energies is given by the mean correlation of the m measurements at the energies E_i^* and E_j^* with an additional contribution accounting for the uncertainty of the geometrical fission-fragment efficiency. This last uncertainty represents the common systematic uncertainty (eq. 15) between the l^{th} and l'^{th} measurements:

$$Corr\left(\langle P_i\rangle\cdot\langle P_j\rangle\right)\cong\frac{1}{m}\sum_{l=1}^{m}Corr\left(P_i^l;P_j^l\right)+\frac{m-1}{m}\cdot\frac{Var\left(\varepsilon_f\right)}{\varepsilon_{fi}\cdot\varepsilon_{fj}}\cdot\frac{\langle P_i\rangle\cdot\langle P_j\rangle}{\sqrt{Var\left(\langle P_i\rangle\right)\cdot Var\left(\langle P_j\rangle\right)}} \tag{22}$$

4. Results

Fig. 8 shows the fission probabilities of ^{242}Am, ^{243}Cm and ^{244}Cm as a function of the compound-nucleus excitation energy and the associated correlation matrices. As described in the previous section, the fission probabilities were obtained as the weighted mean of the fission probabilities measured with the two telescopes. The displayed uncertainties were calculated according to eq. (17). The values of the fission probabilities and the uncertainties are listed in Appendix B. The E^* range considered is limited by the density of target-contaminant peaks in the singles spectrum. As discussed in sections 2 and 3, we assume that the singles spectrum can be interpolated with a smooth exponential function below the contaminant peaks. This assumption is quite reasonable for isolated peaks but becomes less correct as the contaminant peaks get close together. For ^{244}Cm we present also results for excitation energies above 7.5 MeV where the density of target-contaminant peaks becomes significant. The right panels of Fig. 8 show that the correlation between the fission probabilities at different excitation energies increases with excitation energy and reaches up to 90 % at 12 MeV for ^{244}Cm. This increase in the correlation is due to the increase of the intensity of the contaminant peaks with excitation energy, which leads to an enhancement of the systematic error accounting for the uncertainty in the subtraction procedure, see eq. (13).

Our results for the three fission probabilities are compared to the ones by Gavron et al. [9], obtained using the same transfer reactions. Note that the data by Gavron et al. were published in the figures of ref. [9] without specific error bars. Ref. [9] only mentions an estimated uncertainty of about 10% for all the data. For ^{244}Cm our data cover the onset of fission in the excitation-energy region below the neutron separation energy, which is not accessible in neutron-induced measurements. Our results show that the fission probability first increases rather steeply with E^* and, as expected, starts to decrease exactly at S_n, due to the opening of the neutron emission channel. However, in the data by Gavron et al., this drop appears at an excitation energy lower than S_n. Moreover, our results are below those of Gavron et al. between 9 and 12 MeV. These differences could be due to the presence of tungsten in the target used by Gavron et al. [9], which pollutes the singles spectrum down to very low excitation energies and might have not been properly corrected. Our results for ^{244}Cm are also compared to the data by Back et al. [7]. There is a fair agreement between the two data sets at the lowest excitation energies. However, above 5.8 MeV the results by Back et al. are well below our data, even though the trends are similar. Back et al. used the same transfer reaction and the same beam energy as in this work but the ejectiles were detected at 90 degrees with respect to the beam axis. One possible explanation for the observed differences might be that at 90 degrees the contaminant peaks due to light target impurities pollute the singles spectrum down to relative low energies.

For ^{243}Cm, we obtain a slope for the fission threshold that is larger than the one obtained by Gavron et al. An argument to support our results is that the neutron-induced cross section ^{242}Cm(n, f), obtained by multiplying our fission probability of ^{243}Cm with the calculated compound-nucleus formation cross section, follows well the general trend of the data by Vorotnikov et al. [26], see Fig. 7 in ref. [18]. Note that the neutron-induced compound-nucleus formation cross section of ^{243}Cm close to the fission threshold is nearly constant and is equivalent to a simple scaling of the fission probability.

Our results for ^{242}Am agree within the error bars with those by Gavron et al. Our data extend to the second chance fission, where a fraction of the fission events arise from the fission of ^{241}Am. Above 7 MeV the data by Back et al. [24], obtained with the ^{241}Am(d,p) reaction, are about two times lower than our results. According to [25], the (d,p) reaction is problematic because the proton singles spectrum can be polluted by protons originating from the breakup of the projectile. This leads to an overestimation of the single events and to fission probabilities that are systematically too low. In [25], an empirical correction to account for deuteron-breakup effects was applied to the data by Back et al. [24]. However, the comparison of the corrected probability with our data and the one by Gavron et al. shows that this correction is still not sufficient.

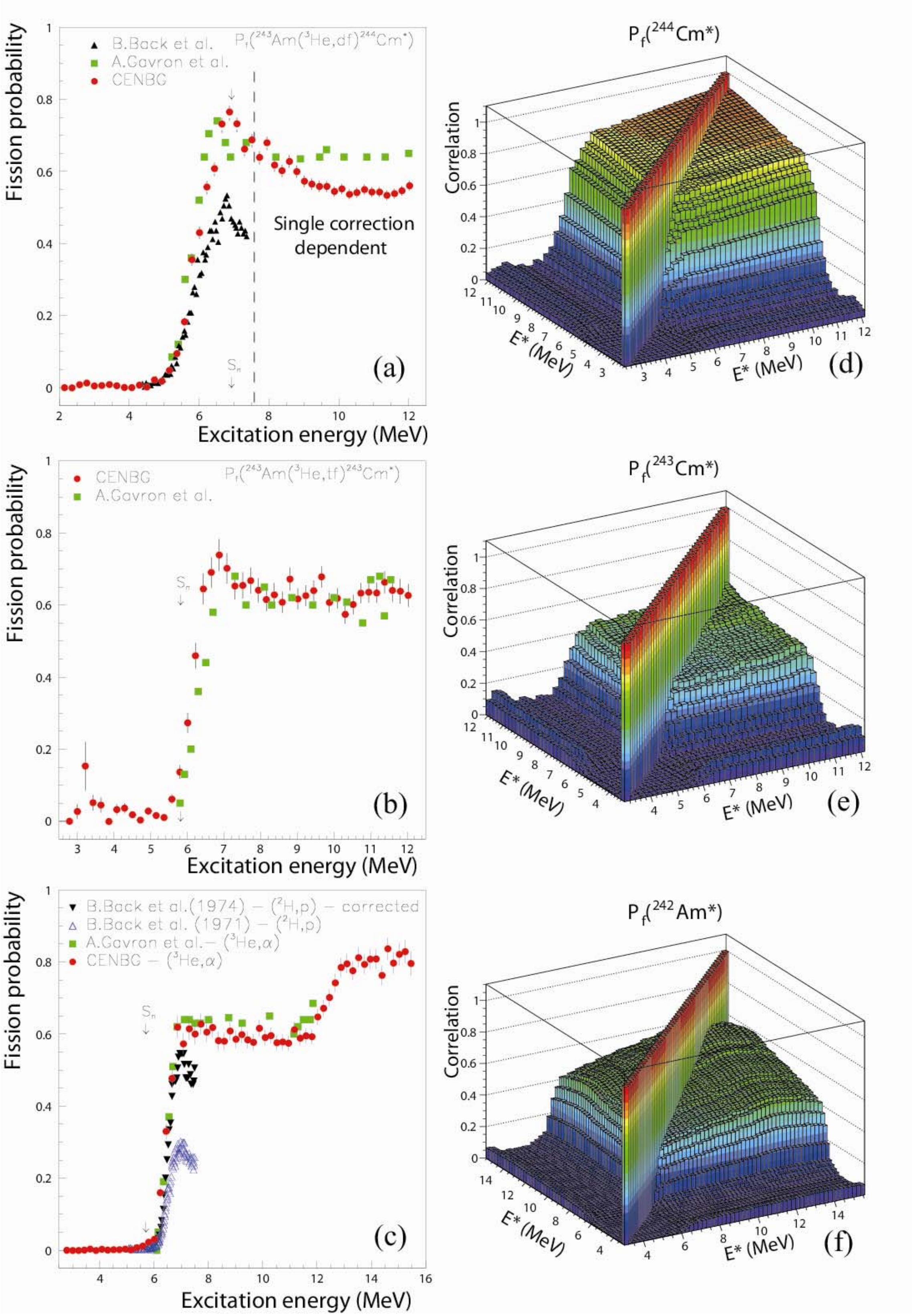

Fig. 8: (Color online) Fission probabilities of the 244Cm* (a), 243Cm* (b) and 242Am* (c) as a function of excitation energy compared to the results by Gavron et al. [9] and by Back et

al. [7, 24, 25]. The dashed line in the upmost left panel represents the E^* above which the singles spectrum is significantly polluted by reactions on target contaminants. The neutron separation energy S_n of each nucleus is indicated by the arrows. (d-e-f) Associated correlation matrices (see section 3.2).

4.1. Sub-threshold structures in ^{243}Cm

Contrary to the data of Gavron et al. and Back et al., our data cover energies well below the fission threshold, see Fig. 8. Interestingly, our results for ^{243}Cm present three clear resonances below the fission threshold. Some sub-threshold structures are also present for ^{244}Cm, but they are much less intense than those observed for ^{243}Cm. No significant structure below the fission threshold is observed for ^{242}Am. One could argue that the lower intensity of the sub-threshold structures in ^{244}Cm is due to the normalization to a larger number of singles events. However, a closer look at the $N_{coinc}(E^*)$ spectra (after subtraction of random coincidences, see section 2.2) of ^{243}Cm and ^{244}Cm revealed that the number of fission events at excitation energies below the fission threshold is much lower for ^{244}Cm than for ^{243}Cm. More precisely, the number of sub-threshold fission events of ^{244}Cm represents only 0.01% of the total number of fission coincidences, whereas in the case of ^{243}Cm it represents 0.16%, which explains the difference in intensity between the sub-threshold peaks of both nuclei.

The details of the subtraction of random-coincidences in the sub-threshold excitation-energy region of ^{243}Cm are illustrated in Fig. 9. The (red) dashed histograms represent the spectra that result from selecting the events in the time-coincidence window (Fig. 6) for each telescope. We subtracted from these spectra the spectra of random coincidences, which are given by the ejectile spectrum N_{eje} (see eq. 8) normalized to the total number of random coincidences. Because of the very low number of random coincidences, the difference between the coincidence spectra before and after the subtraction of random coincidences is hardly appreciable. Fig. 9 shows that the random-coincidences spectra of both telescopes (blue full lines) do not show any significant structure that could explain the observed resonances.

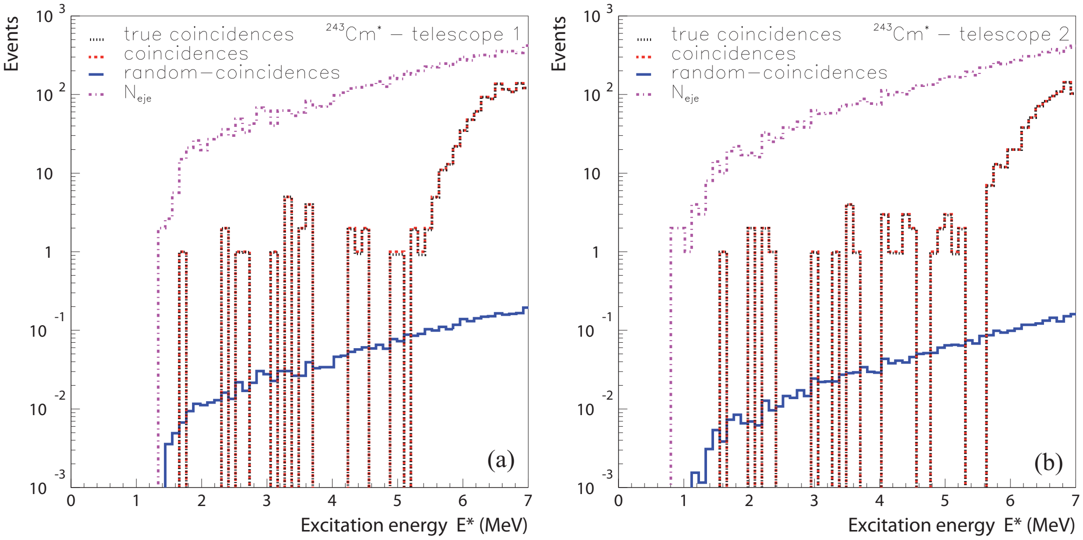

Fig. 9: (Color online) Number of fission-fragment-triton coincidences before (red dashed line) and after (black full line) subtraction of random coincidences. The spectrum of ejectiles N_{eje} is represented by the dashed-dotted lines and the random-coincidences spectrum by the blue full lines.

As discussed in section 3, the final fission probability is the weighted mean of the probabilities obtained with the two telescopes. When determining the average probability the structures below 2.7 MeV vanish because their positions in the two telescopes are different. However, the positions of the structures above 2.7 MeV are very similar in both telescopes and lead to an average fission probability significantly above zero, as seen on the left part of Fig. 10. Unfortunately, the statistics at such low excitation energies is too low and the fission fragment anisotropy cannot be measured. Therefore, to calculate the fission probability we used the same fission-detection efficiency as for the higher excitation energies. However, we recall that, due to the large solid angle of our fission detector, the influence of the angular anisotropy on the effective efficiency is relatively weak. Moreover, one would need effective efficiencies greatly above 100% to make the structures disappear.

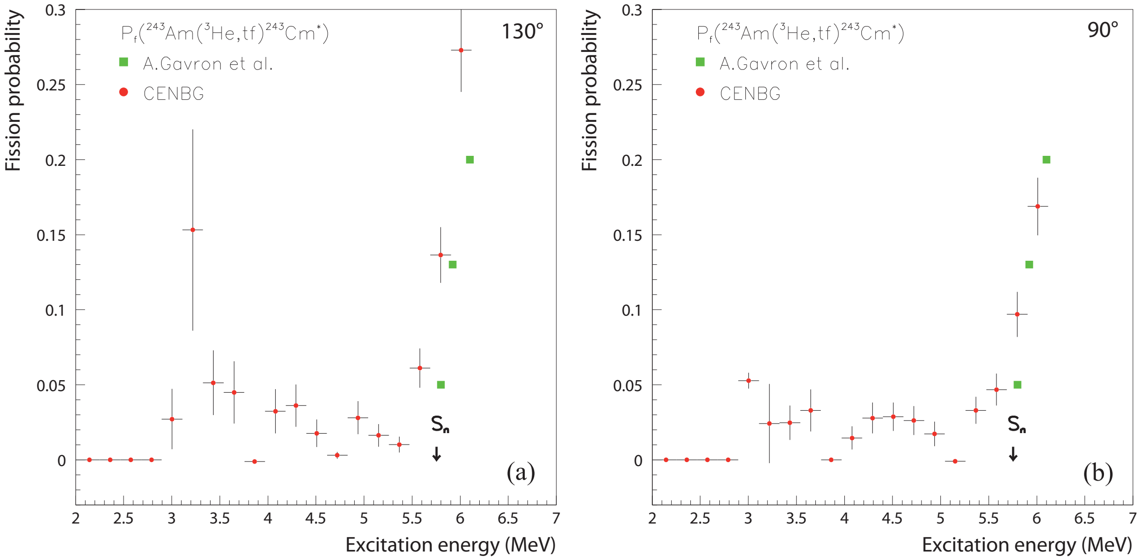

Fig. 10: (Color online) Fission probability of ^{243}Cm obtained with the ^{243}Am(^{3}He,t) reaction as a function of excitation energy in the proximity of the fission threshold. On the left we show the results obtained with the telescopes placed at 130 degrees (a) and on the right with the telescopes placed at 90 degrees (b) with respect to the beam axis. The neutron separation energy S_n is indicated.

We performed a test experiment with the same setup but the telescopes placed at 90 degrees. The right part of Fig. 10 illustrates the average fission probability obtained with the two telescopes located at 90 degrees. It shows clear structures at excitation energies that are very close to the positions of the sub-threshold structures observed with the telescopes placed at 130 degrees, although there are some differences in the shape. In particular, the data at 90 degrees do not show a double-peak structure between 4 and 5 MeV. The presence of peaks below the fission threshold at nearly the same positions for both detection angles supports the hypothesis that these structures come from fission events in ^{243}Cm. Indeed, if the peaks were due to non-corrected random coincidences with some light or medium-mass contaminants, their positions would considerably vary when changing the telescope angle from 130 to 90 degrees.

To our knowledge, it is the first time that sub-threshold structures have been observed for ^{243}Cm. The presence of these resonances was a rather unexpected result of this experiment, whose main objective was the determination of fission probabilities at the fission threshold and above.

5. Statistical-model calculations

The aim of this section is to extract information on fission barriers by comparing our data to statistical-model calculations. In this theoretical analysis we will not consider directly the resonances observed for ^{243}Cm because our experimental conditions (excitation-energy bin of 210 keV and limited statistics) are not well adapted to provide the required precision for a quantitative analysis.

5.1. Description of the model

We assume that the considered transfer reactions lead to the formation of a compound nucleus. The decay can then be described with the statistical model, which takes into account the competition between the different decay modes: gamma emission, neutron emission and fission. We also assume a double-humped fission barrier. As we have not observed any relevant structure for ^{244}Cm and ^{241}Am and we do not treat the structures observed for ^{243}Cm, the average fission probability is computed in the complete damping limit [7]. In this limit, the energy from the pure fission motion is redistributed into internal excitations in the second well and statistical equilibrium can be assumed. This means that resonant barrier penetration is neglected and the transmission through the two barriers can be treated independently, i.e. the fission process can be viewed as the crossing of the inner barrier (*A*) followed by the crossing of the outer barrier (*B*). At the corresponding saddle-point deformations (β_A and β_B), the barrier shapes are approximated by inverted parabolas, which define the barrier heights and curvatures of the inner (E_A, $\hbar\omega_A$) and outer (E_B, $\hbar\omega_B$) barrier.

Within the frame of the statistical model, the average fission probability may be written as:

$$< P_f(E^*) >= \sum_{J^\pi} \alpha(E^*,J,\pi) \frac{\langle N_f \rangle}{\sum_i \langle N_i \rangle} f(E^*,J,\pi) \qquad (23)$$

where:

-$\alpha(E^*, J, \pi)$ is the average probability for populating a compound state of angular momentum *J* and parity *π*. This distribution is normalized so that $\sum_{J^\pi} \alpha(E,J,\pi)=1$.

-$\frac{\langle N_f \rangle}{\sum_i \langle N_i \rangle}$ is the average fission probability of a compound state J^π at E^*. N_i is the effective number of open decay channels which are populated by gamma emission ($i = g$), neutron emission ($i = n$) and fission ($i = f$). This quantity is related to the average decay width $\langle \Gamma_i(E^*, J, \pi) \rangle$ and level spacing $\langle D_{gs}(E^*, J, \pi) \rangle$ of the compound nucleus at the ground-state deformation by the relation: $\langle N_i(E^*, J, \pi) \rangle = 2\pi \frac{\langle \Gamma_i(E^*, J, \pi) \rangle}{\langle D_{gs}(E^*, J, \pi) \rangle}$.

-$f(E^*, J, \pi)$ is a level-width fluctuation factor which takes into account that we have replaced in eq. (23) the average expression by the average of its terms: $\left\langle \frac{N_f}{\sum_i N_i} \right\rangle = f(E^*, J, \pi) \frac{< N_f >}{\sum_i < N_i >}$. This factor has been calculated using the approach proposed in ref. [24]. In the present work, the fluctuation factor reduces the calculated fission probabilities by at most 10%.

For fission, the number of open channels is given by the number of transition states on top of the barriers x (= A or B) weighted with the corresponding barrier transmission coefficient:

$$\langle N_{f_x}^{J,\pi}(E^*) \rangle = \sum_K \frac{1}{1 + \exp[\frac{2\pi}{\hbar\omega_x}(E_x + E_x^{K\pi} - E^*)]} + \int_{-\infty}^{E^* - E_i} \frac{\rho_x(E^* - (E_x + \varepsilon), J, \pi)}{1 + \exp[-\frac{2\pi}{\hbar\omega_x}\varepsilon]} d\varepsilon \tag{24}$$

Here, the summation accounts for discrete transition states on top of the barrier at energy $E_i^{K\pi}$ and the integral for transition states in the continuum. The discrete transition states are characterized by the quantum number K, that results from the projection of J on the symmetry axis. ε and ρ_i are the kinetic energy in the fission degree of freedom and the level density of compound states (J^π) at the top of the barrier of height E_i, respectively.

After the penetration of barrier E_A, the excited nucleus can decay by neutron emission, gamma emission, penetration of the first barrier, or penetration of the second barrier which leads to fission [7]. Our calculations show that, due to the relatively modest excitation energies considered (maximum $E^* \approx 15$ MeV), neutron and gamma emission from compound states in the super-deformed well between the two barriers can be neglected. In this case, the effective number of fission channels on top of the double-humped fission barrier is:

$$\langle N_f^{J,\pi}(E^*) \rangle \approx \langle N_{f,A}^{J,\pi}(E^*) \rangle \cdot \frac{\langle N_{f,B}^{J,\pi}(E^*) \rangle}{\langle N_{f,A}^{J,\pi}(E^*) \rangle + \langle N_{f,B}^{J,\pi}(E^*) \rangle} \tag{25}$$

We consider that neutron emission does not modify the deformation of the compound nucleus and that it occurs from the first well of nucleus A to the first well of nucleus A-1. Under these conditions, the number of open channels for neutron emission is given by:

$$\begin{aligned}\left\langle N_n^{J,\pi}(E^*)\right\rangle &= \sum_{E'J'\pi'}\sum_{j=|J-J'|}^{J+J'}\sum_{l=|j-1/2|}^{j+1/2}\delta(\pi,\pi',(-1)^l)\cdot T_l^j(E_n)\\ &+\int_{E_d}^{E^*-S_n}\sum_{j=|J-J'|}^{J+J'}\sum_{l=|j-1/2|}^{j+1/2}\delta(\pi,\pi',(-1)^l)\cdot\rho(E',J',\pi')\cdot T_l^j(E_n)\cdot dE'\end{aligned} \tag{26}$$

Both, the discrete and the continuous levels (E', J', π') of the residual nucleus have been considered. E_d is the excitation energy in the residual nucleus where the continuum starts. $\delta(\pi,\pi_f,(-1)^l)$ is the parity-conservation factor. $T_l^j(E_n)$ is the transmission coefficient for emission of a neutron with kinetic energy $E_n = E^* - S_n - E'$, orbital angular momentum l and channel spin $j = l + s$ (s being the intrinsic spin of the neutron). The transmission coefficients have been calculated with a Lane-consistent semi-microscopic [27] deformed [28] optical model potential, built using deformed radial nuclear densities calculated in the Hartree–Fock–Bogoliubov framework with the Gogny D1S interaction [29]. In this work, the structure of the discrete states of the relevant residual nuclei has been taken from [30-32]. When the experimental information was scarce (e.g. for ^{242}Cm), levels were generated by assuming the same structure as in neighboring nuclei.

We assume that gamma emission takes place between two states in the first well of the compound nucleus and that only electric dipole transitions (E1) contribute to the γ-decay channel. According to the Weisskopf strong coupling model, the average number of open channels that proceed through γ-decay from initial compound states (J^π) at excitation energy E^* is:

$$\left\langle N_g^{J\pi}(E^*)\right\rangle = C\cdot\sum_{J''=J-1}^{J+1}\int_0^{E^*}\rho(E'',-\pi,J'')\cdot(E^*-E'')^3\cdot dE'' \tag{27}$$

The summation runs over the continuous final states (E'', J'', $\pi'' = -\pi$) of the residual nucleus after emission of a γ-ray of energy $E_\gamma = E^* - E''$ only because the contribution from discrete final states is negligible. The constant C is adjusted to reproduce the experimental neutron-induced average γ-decay width at the neutron binding energy (S_n) of the relevant compound nuclei [33]. This normalization implies the assumption that the γ-decay widths are independent of spin and parity, which appears to be reasonable for the heavy nuclei studied in this work [7, 24]. We have also considered a more sophisticated description for the gamma-strength function based on a Lorentzian [34] but this has essentially no impact on our results.

5.1.1. Level densities

As discussed above, the fission probability depends strongly on the nuclear level densities $\rho(E^*, J, \pi)$ at different elongations of the fissioning nucleus (ground state, first and second barriers), as well as on those of the residual nuclei after neutron emission. The level densities used in this work can be represented as the product of the intrinsic level density and the density of collective excitations. The intrinsic level density ρ_{int} has been calculated with the phenomenological version of the Generalised Superfluid model of Ignatyuk. A detailed description of this model can be found in [35].

In this model, the most important parameter is the level-density parameter, whose dependence on shell effects and E^* above the critical pairing energy is given by:

$$a(E^*, N, Z) = \tilde{a}(N, Z)\left(1 + \frac{\Delta S}{E^*} f(E^*)\right) \tag{28}$$

with

$$f(E^*) = 1 - \exp(-\gamma E^*) \tag{29}$$

and

$$\gamma = 0.4 A^{-\frac{1}{3}} \tag{30}$$

Here, ΔS is the ground-state shell correction, defined as the difference between the experimental nuclear mass and the liquid drop mass calculated at the corresponding deformation. $\tilde{a}$ is the asymptotic value of the level density parameter at high excitation energy. For the ground-state deformation, this asymptotic level density parameter takes the form [35]:

$$\tilde{a} = 0.073 A + 0.115 A^{\frac{2}{3}} \tag{31}$$

Contrary to $\tilde{a}$ at ground state deformations, the magnitude of $\tilde{a}$ at larger deformations has not been constrained with experimental data. In addition, there are large uncertainties in the theoretical predictions for the surface and volume coefficients needed to quantify the variation of the level density parameter with deformation. For this reason, in this work we have treated the asymptotic values of the level density parameters at the barriers, $\tilde{a}_A$ and $\tilde{a}_B$, as free parameters.

We consider that only rotational states contribute to the density of collective states. Following the prescription of Bohr and Mottelson [36], the rotational states for a prolate axially symmetric deformation have been built on each intrinsic level described above. Assuming that the rotational energies are small compared to the total excitation energy, the level density takes the form:

$$\rho(E, J, \pi) \approx \frac{1}{2} C_{coll} \frac{\rho_{int}}{\sqrt{8\pi}\sigma_{\|}(E^*)} \sum_{K=-J}^{J} \exp\left[-\frac{K^2}{2\sigma_{\|}^2(E^*)} - \frac{J(J+1) - K^2}{2\sigma_{\perp}^2(E^*)}\right] \tag{32}$$

where the factor 1/2 accounts for the assumption of equal number of levels with positive and negative parity. $\sigma_{\|}$ and $\sigma_{\perp}$ represent the deformation-dependent spin cutoff factors, which are closely related to the nucleus moment of inertia parallel and perpendicular to the nuclear symmetry axis. The relevant moment of inertia at the ground state and at the inner- and outer-barrier deformations have been computed from the set of prolate deformations calculated by Howard and Möller [37]. The density of rotational states is known to vary with deformation. It is now well established that the breakdown of various symmetries leads to a significant enhancement of the level densities at the barrier deformations [36]. The factor C_{coll} takes different values depending on the deformation. For deformations with axial asymmetry $C_{coll} = \sqrt{8\pi}\sigma_{\|}(E^*)$ and for axial symmetric but reflection asymmetric shapes $C_{coll} = 2$ [38].

5.1.2. Discrete transition states

For the nuclei of interest in this work, the information on the properties of the transition states at the barriers is very scarce. Fission-probability measurements combined with measurements of fission-fragment angular distributions can provide the angular momentum J and its projection K of the transition states. Unfortunately, such measurements were not performed in the past for the relevant nuclei here. Note that the angular distributions that we measure are not adapted to extract precise information on the transition states due to the large angular uncertainty of our data of approximately $\Delta\theta \approx 30°$ and to the limited statistics. Our measurements can only be used to confirm the low sensitivity of the fission efficiency of our detector to the fission-fragment angular anisotropy.

^{244}Cm				**^{243}Cm**				**^{242}Am**				**^{241}Am**			
Inner Barrier		Outer Barrier		Inner Barrier		Outer Barrier		Inner Barrier		Outer Barrier		Inner Barrier		Outer Barrier	
K^π	E	K^π	E	K^π	E	K^π	E	K^π	E	K^π	E	K^π	E	K^π	E
0+	0	0+	0	1/2+	0	1/2+	0	1-	0	1-	0	5/2-	0	5/2-	0
2+	0.2	0-	0.25	5/2+	0.08	3/2+	0.08	0-	0.044	0-	0.044	3/2+	0.02	3/2+	0.02
0-	0.4	2+	0.5	1/2-	0.05	5/2+	0.02	5-	0.049	5	0.049	1/2+	0.04	1/2+	0.04
				3/2-	0.1			6-	0.170	6-	0.170				
								1-	0.220	1-	0.220				
								3-	0.242	3-	0.242				
								2-	0.288	2-	0.288				

Table 4: Spectrum of discrete transition states used in this work. Given is the energy in MeV of the transition states above the corresponding fission barrier.

Gavron et al. [9] used the calculated spectrum of transition states of ^{240}Pu, which they took from [25], for all the nuclei they investigated. For odd-odd nuclei no discrete transition states were considered. The situation is somewhat less complicated for even-even nuclei, because one can make a reasonable guess of the properties of the transition states at the barriers from the evolution with deformation of the low-lying rotational and vibrational states from the ground state. The spectra of transition states used in this work for $^{243,\,244}$Cm and ^{241,242}Am are given in Table 4. The energies of the states were slightly tuned to best reproduce the data. The inclusion of additional states did not have any impact on the results of the calculations. The energies of the transition states for ^{244}Cm at the first barrier are very close to the ones used in [7], which were considered the same for the inner and outer barriers. Our spectra are in general good agreement with the generic recommended values given by RIPL3 [33]. There are only significant differences in the energies of the 1/2$^-$ state at the inner barrier and of the 5/2$^+$ state at the outer barrier of the even-odd ^{243}Cm, and in the spectrum at the inner barrier of ^{241}Am.

Each of these transition states is the band head of a rotational band with the rotational parameter $\frac{\hbar^2}{2\Im_x}$, $\Im$ being the moment of inertia at each barrier. We have taken $\frac{\hbar^2}{2\Im_A}$ = 7 keV and $\frac{\hbar^2}{2\Im_B}$ = 5 keV [25]. Axial symmetry breaking induces $(2J + 1)$ rotational levels for each value of the total angular momentum J. Levels of opposite parity (but equal energy) are added to the intrinsic levels in order to account for reflection asymmetry. In this way, a set of discrete transition states was built up to the pairing gap: 2Δ for ^{244}Cm and Δ for ^{243}Cm and ^{241}Am, where we have assumed $\Delta = \frac{12}{\sqrt{A}}$. Beyond the pairing gap, the continuous level density described in the previous section was assumed for both nuclei.

5.1.3. Determination of $\alpha(E^*, J, \pi)$

While it is possible to calculate the angular-momentum and parity distributions populated in neutron-induced reactions using optical potentials, this is by far not the case when the compound nucleus is formed in a transfer reaction (see [17]). Transfer reactions populate single-particle states, such as single neutron states in the (d,p) reactions, single proton states in the (^{3}He,d) reaction and single neutron-hole states in the (^{3}He,^{4}He) reactions. This quite simple picture is valid at low excitation energies, and has been extensively used in the past in nuclear-structure studies. However, in the excitation-energy region of interest in this work ($E^*>S_n$), these single-particle states are strongly mixed with the highly dense and complex compound-nuclear states, whose decay is described by the statistical model. In other words, the strength of the particular single-particle states populated by the direct reaction “spreads out” over a large number of compound levels [39]. Therefore, one can imagine the reactions studied in this work as two-step processes where the single particle states initially populated by the transfer reactions readily mix with the continuum of compound levels that have the same quantum numbers (J^π), leading eventually to the formation of a compound nucleus. It is difficult to theoretically estimate how the initial single-particle states are fragmented into the complex many-body states in the continuum and usually different approximations are used [40, 41]. Similarly to [7], in this work we assume that the angular-momentum distribution α is independent of E^*, and that the spreading width is directly proportional to the density ρ of compound-nuclear levels with J^π:

$$\alpha(J,\pi) = Q(J,\pi)\rho(J,\pi) \tag{33}$$

where $Q(J, \pi)$ gives the probability of feeding the single-particle level J^π by the transfer reaction. The final spin J is given by:

$$\vec{J} = \vec{I} + \vec{l} + \vec{s} = \vec{I} + \vec{j} \tag{34}$$

where I is the target spin, l is the orbital angular momentum transferred in the reaction and s is the intrinsic spin of the transferred particles. l and s combine to give the channel spin j. For a given J we have:

$$\alpha(J,\pi) = \rho(J,\pi) \sum_{j=|J-I|}^{J+I} \sum_{l=|j-s|}^{j+s} \frac{\sigma(l)\delta(\pi_I, \pi_s, (-1)^l)}{N_l} \tag{35}$$

where $\sigma(l)$ is the reaction cross section (dimensionless) as a function of transferred orbital angular momentum l. In the above eq., the double summation takes into account all possible ways to generate J from $j + I$ and all possible ways to generate j from l + s. The number of these couplings is given by:

$$N_l = \sum_{j=|J-I|}^{J+I} \sum_{l=|j-s|}^{j+s} 1 \tag{36}$$

The quantity $\sigma(l)$ is not known for the reactions of interest in this work. Instead of using orbital angular-momentum distributions of arbitrary shapes, we have used the neutron-induced distributions $\sigma_n(l)$ populated at different neutron energies E_n. The latter distributions can be calculated with the transmission coefficients $T_l^j(E_n)$ used to determine the number of open channels for neutron emission. Figure 11 shows the calculated distributions at different neutron energies for ^{242}Am. The distributions for ^{243}Cm and ^{244}Cm are very similar. In this way, we investigated the influence of very different angular-momentum distributions on the properties of the fission barriers.

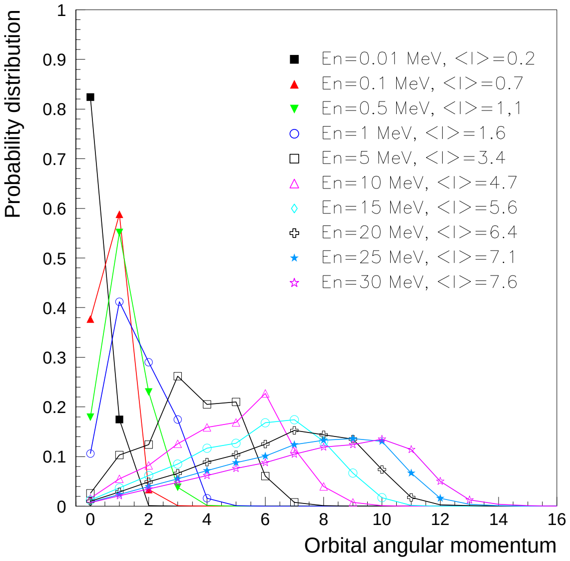

Fig. 11: (Color online) Calculated neutron-induced orbital angular-momentum distributions $\sigma_n(E_n, l)$ populated in the reaction n + ^{241}Am at different incident neutron energies, E_n.

5.2. Comparison between theory and experiment

Calculated fission probabilities from the model described above have been compared to the fission probabilities measured in this work to deduce the heights and curvatures of the inner and outer barriers, which were treated as adjustable parameters. We assume that the inner barrier (E_A) is axially asymmetric, while the outer one (E_B) is axially symmetric but reflection asymmetric [42]. Calculations were also performed assuming an axial symmetric shape at the inner barrier, but in this case it was not possible to fit the data for ^{243}Cm and ^{242}Am.

As mentioned before, for ^{244}Cm the region above approximately 7.5 MeV suffers from the presence of target contaminants and the shape of the fission probability depends on the assumption made for the shape of the singles spectrum below the contaminant peaks. Therefore, we have performed two separated fits, one including only the data below 7.5 MeV and the other considering all the available data.

5.2.1. Sensitivity of the fission-barrier parameters to the transferred angular-momentum distribution

For ^{244}Cm, the calculated fission probabilities were rather insensitive to the angular-momentum distribution except for the region between the neutron separation energy and about 8 MeV. This region is very sensitive to the shape of the neutron-emission probability. When the transferred angular momentum is low, neutron emission to the low-lying states of ^{243}Cm is favored and the neutron-emission probability sets in rather steeply. This leads to a strong decrease of the fission probability, that we do not observe in our data. This is astonishing, given the good agreement between our results for the ^{243}Cm(n,f) and the neutron-induced data in the vicinity of S_n, see ref. [18]. The reason for this discrepancy may be some deficiency in the experimental data (including the most recent neutron-induced data) or/and a poor knowledge of the structure of ^{243}Cm at the lowest energies. The best fit to the data below 7.5 MeV and to the ensemble of data was obtained with the distribution $\sigma_n(E_n=30\text{ MeV}, l)$ with $\langle l \rangle \approx 7.6$. The different fits give fairly similar results for E_A and the two barrier curvatures, with differences below 200 keV. The second barrier shows a stronger sensitivity to the transferred angular momentum and we find a difference of about 300 keV between the fits.

Similarly to the ^{244}Cm case, we could not reproduce the experimental data in the vicinity of the fission threshold of ^{243}Cm using the transferred angular-momentum distributions with the lowest spins corresponding to $E_n \leq 1$ MeV. This may be due to the lack of knowledge on the properties of the low-lying states in the even-even ^{242}Cm. We recall that for ^{242}Cm the structure information is very scarce and we have assumed the levels of neighboring nuclei. In addition, one should also keep in mind that the complete damping limit is not the appropriate frame to treat this nucleus, which presents clear structures at low excitation energies. We found better agreement with the data when considering the distributions $\sigma_n(E_n>10\text{ MeV}, l)$. The best agreement was found for $\sigma_n(E_n=15\text{ MeV}, l)$ with $\langle l \rangle \approx 5.6$, but there are relatively small differences between the calculations using the distributions corresponding to $\sigma_n(E_n>10\text{ MeV}, l)$. The calculations with $\sigma_n(E_n>10\text{ MeV}, l)$ gave results for E_A, E_B and $\hbar\omega_A$ that agree within less than 100 keV. Yet, the differences for $\hbar\omega_B$ reach 300 keV.

The calculations for ^{242}Am are less sensitive to the transferred angular momentum than the calculations for ^{243}Cm and ^{244}Cm. Above approximately $E^* = 7.5$ MeV we found essentially no difference between the fission probabilities calculated with the different $\sigma_n(E_n, l)$ distributions for ^{242}Am. The calculation with the orbital angular momentum distribution at $E_n = 1$ MeV (corresponding to $E^* = 6.5$ MeV and to $<l> \approx 1.6$) gave a slightly better agreement with the experimental data. We observed a very weak sensitivity of the fission barrier heights to the shape of $\sigma_n(E_n, l)$. A maximum difference of 50 keV was found between the inner barrier height deduced with $\sigma_n(E_n=1 \text{ MeV}, l)$ and $\sigma_n(E_n=30 \text{ MeV}, l)$. The fluctuations associated to the outer barrier height and the curvatures were within 200 keV.

5.2.2. Results

The best fits to the data are shown in Fig. 12. For ^{244}Cm we show the calculation assuming axial symmetry at the inner barrier and the calculation assuming axial asymmetry with the angular-momentum distribution corresponding to $<l> \approx 7.6$. The two fits, including only the data below 7.5 MeV and all the available data, show a similar agreement with the data. Only the fit considering all the available data is plotted in Fig. 12a. We find an overall good agreement between calculations and experimental data for the three nuclei. The values of the barrier parameters from the best fits (those with the minimum χ^2 deviation) are listed in Table 5.

We have made a considerable effort to estimate the uncertainty of the 6 fit parameters (the 4 barrier parameters and the 2 asymptotic level-density parameters) in a rigorous way. For each fissioning nucleus we performed one million of calculations with values for the 6 parameters that were randomly and independently sampled from uniform probability distributions. The uncertainty tabulated in Table 5 corresponds to half of the total range spanned by the values of the parameters for which $\chi^2 \leq \chi^2_{\min} + D$. The quantity D has been determined according to the procedure described by Avni [43]:

$$\text{Probability}[\chi^2(q \text{ fit parameters}) \leq D] = CL \tag{37}$$

where CL is the confidence level. That is, $D(CL, q)$ is the χ^2 value that one finds from the table of a χ^2 distribution with q degrees of freedom. In our case we have $q = 6$ parameters and we have chosen $CL = 99\%$, therefore $D(CL{=}0.99, q{=}6) = 16.8$. In other words, the range of parameter values for which $\chi^2 \leq \chi^2_{\min} + 16.8$ includes the true values of the parameters with 99% probability. We have tested this criterion following the procedure of Avni [43], i.e. by simulating a number of experimental fission-probability measurements with known input values of the barrier and level-density parameters. In 99 % of the cases the interval defined by the values of the fitted parameters with the uncertainty limits given by the condition $\chi^2 \leq \chi^2_{\min} + 16.8$ included the input values.

The uncertainties of the barrier parameters given in Table 5 show that our data for ^{244}Cm mainly constrain the height of the outer barrier. For this nucleus we obtain a smaller difference between the two barrier heights (under the assumption of axial asymmetry). The results obtained when only the data below 7.5 MeV are fitted agree within the uncertainties with the results obtained fitting the whole range of excitation energy.

The uncertainties given in Table 5 for ^{243}Cm, ^{242}Am and ^{241}Am show that our data well constrain the height and the curvature of the first fission barrier, while they weakly constrain the barrier parameters of the second barrier. For these nuclei our data require a first barrier that is significantly higher than the second barrier. In this situation, the height of the first barrier dominates the onset of the fission probability, because $<N_{f,A}> << 1$, see eq. (25). Only at higher excitation energies there is some influence of the second barrier, which remains anyhow rather weak, due to the significant difference between the two barrier heights.

In Table 5 our results are compared to the ones by Back et al., Gavron et al. and to the empirical systematics by Bjornholm and Lynn [42] and RIPL3 [33]. The values for $\hbar\omega_{\mathrm{A}}$ and for E_B by Gavron et al. are in parenthesis because they "should be regarded with extreme caution", as stated by the authors themselves. Our results for the first barrier of ^{244}Cm, using the assumption that the inner barrier is axial asymmetric, are in good agreement with the ones of Gavron et al. The differences between our data and that of Gavron et al. at the highest excitation energies (see Fig. 8) are not relevant for the determination of E_A because E_A is mainly determined by the probability at the fission threshold. Our value for the first barrier of ^{244}Cm is also in good agreement with the one by Back et al., despite the important differences between fission probabilities on which the two analyses are based. Obviously, if we would fit our model calculations to the data by Back et al. we would obtain a higher inner barrier. The reason for the good agreement in the barrier values might be that Back et al. did not consider collective enhancement in the level density, which results in a significant increase of the level density. We may speculate that, with a much higher level density, Back et al. would have obtained a significantly higher barrier. Our results for E_A assuming axial asymmetric shapes are in good agreement with the recommended values by RIPL3, whereas our results assuming axial symmetry are in agreement with the systematics by Bjornholm and Lynn. The calculations assuming axial asymmetric shapes at E_A give a value for E_B that is higher than the value given by RIPL3.

For ^{243}Cm, our results (see Fig.12b) for E_A agree within the uncertainties with the results by Gavron et al. They observed that for this nucleus E_A was particularly sensitive to the used level-density description, leading to the large uncertainty of 500 keV given in Table 5. Note that the model calculation by Gavron et al. did not fit well the data in the excitation-energy region around 7 MeV. Our results for E_A and $\hbar\omega_x$ are in good agreement with Bjornholm and Lynn, but our value for E_A is somewhat higher than the value given in RIPL3.

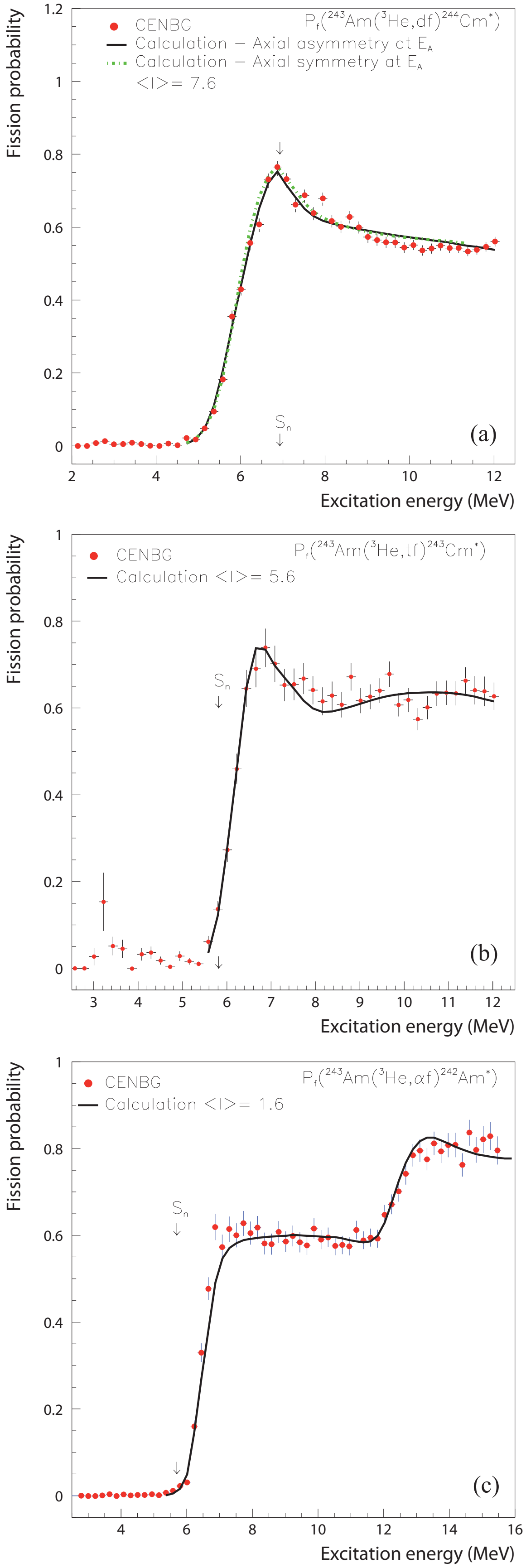
Fission probability
CENBG
$P_f(^{243}Am(^3He,df)^{244}Cm^*)$
Calculation – Axial asymmetry at E_A
Calculation – Axial symmetry at E_A
<I>= 7.6
S_n
(a)
1.2
1
0.8
0.6
0.4
0.2
0
2
4
6
8
10
12
Excitation energy (MeV)
Fission probability
CENBG
$P_f(^{243}Am(^3He,tf)^{243}Cm^*)$
Calculation <I>= 5.6
S_n
(b)
1
0.8
0.6
0.4
0.2
0
3
4
5
6
7
8
9
10
11
12
Excitation energy (MeV)
Fission probability
CENBG
$P_f(^{243}Am(^3He,\alpha f)^{242}Am^*)$
Calculation <I>= 1.6
S_n
(c)
1
0.8
0.6
0.4
0.2
0
4
6
8
10
12
14
16
Excitation energy (MeV)

Fig. 12: (Color online) Experimental fission probabilities (full circles) compared to statistical-model calculations, see text for details.

Fissioning nucleus	**Reference**	**E_A [MeV]**	**$\hbar\omega_A$ [MeV]**	**E_B [MeV]**	**$\hbar\omega_B$ [MeV]**
^{244}Cm (S_n=6.8 MeV)	This work (Fit to data E*< 7.5 MeV)	6.25±0.40	0.8±0.3	5.6±0.2	0.40±0.15
	This work (Fit to all the data)	5.70±0.55	1.10±0.45	5.85±0.20	0.75±0.20
	This work (E_A axial symmetric)	5.90±0.14	0.80±0.15	4.0 ± 0.7	1.0±0.4
	Gavron et al.[9]	6.2±0.2	(0.9)	(4.6)	-
	Back et al. [7]	6.12±0.2	0.90±0.10	<4.9	-
	Bjornholm and Lynn [39]	5.8±0.2	1.04	4.3±0.3	0.60
	RIPL3 [30]	6.18	0.9	5.10	0.6
^{243}Cm (S_n=5.7MeV)	This work	6.6±0.1	0.71±0.13	5.42±0.85	1±0.5
	Gavron et al. [9]	5.95±0.50	(0.6)	(5.5)	-
	Bjornholm and Lynn [39]	6.4±0.3	0.80	-	0.52
	RIPL3 [30]	6.33	0.7	5.4	0.5
^{242}Am (S_n=5.5 MeV)	This work	6.4±0.1	0. 60±0.13	5.8±0.7	0.7±0.3
	Gavron et al. [9]	6.4±0.2	(0.38)	(5.05)	-
	Back et al. [25] (d,p) corrected	6.38±0.20	0.50±0.10	-	-
	Back et al. [24]	6.35±0.15	0.6±0.15	-	-
	Bjornholm and Lynn [39]	6.5±.0.2	0.65	5.4±0.3	0.45
	RIPL3[30]	6.32	0.60	5.78	0.40
^{241}Am (S_n=6.6 MeV)	This work (from second-chance fission of ^{242}Am)	6.6±0.13	0.7±0.2	4.6±0.7	0.6±0.3
	Gavron et al. [9]	6.0±0.2	(0.55)	(5.1)	-
	Back et al. [25]	6.0±0.2	0.8±0.1	-	-
	Bjornholm and Lynn [39]	6.0±0.2	0.8	5.1±0.3	0.52
	RIPL3[30]	6.0	0.8	5.35	0.5

Table 5: Fission-barrier parameters obtained in this work compared to the values from other fission-probability analysis and empirical systematics. The values by Gavron et al. in parentheses are subject to important uncertainties, according to the authors.

The value of E_A obtained for ^{242}Am (see Fig.12c) agrees well with the result by Gavron et al. We find also very good agreement with the results by Back et al., despite the significant lower fission probabilities, in particular for the uncorrected data [24]. This may be due to the fact that in [24] additional information on shape isomer half lives and isomeric ratios was used to constrain the barrier parameters and curvatures. Our results are also in good agreement with Bjornholm and Lynn and RIPL3. For ^{241}Am our result for E_{A} is somewhat higher than the other published values.

Table 6 shows the values of $\tilde{a}_x/\tilde{a}_n$ that best reproduced the data, where $\tilde{a}_x$ is the asymptotic level density parameter at the fission barrier and $\tilde{a}_n$ at the ground state of the corresponding residual nucleus after neutron emission (whose value follows from eq. 31). Our results are affected by rather large uncertainties and agree within the error bars with the starting values recommended by RIPL3 (between 1.05 and 1.07) [33].

Fissioning Nucleus	$\frac{\tilde{a}_A}{\tilde{a}_n}$	$\frac{\tilde{a}_B}{\tilde{a}_n}$
^{244}Cm	0.95±0.30	1.18±0.06
^{243}Cm	1.19±0.16	1.08±0.24
^{242}Am, ^{241}Am	1.16±0.50	1.26±0.10

Table 6: Values of the asymptotic level density parameters at the barriers used in this work. The values for ^{244}Cm correspond to the fit to the ensemble of data.

6. Conclusion

We have measured the fission probabilities of ^{242}Am, ^{243}Cm and ^{244}Cm induced by few-nucleon transfer reactions between a ^{3}He beam and a ^{243}Am target. The details of the experimental set-up and the data analysis have been described. We have presented a detailed uncertainty analysis. To our knowledge, it is the first time that such a rigorous uncertainty study has been performed on transfer-induced fission probabilities. This analysis shows that the covariance between the single and coincidence events has a significant impact on the final uncertainty of the fission probability. We have also carefully investigated the correlation between the experimental data at different excitation energies. This correlation is caused by the fission-detection efficiency, which is given by the solid angle of the fission-detector and is constant for all excitation energies, and by the target-contaminant subtraction. The increase of the correlation with excitation energy is due to the target-contaminant subtraction.

We have compared our fission probabilities to those by Gavron et al. [9], obtained using the same transfer reactions and similar experimental conditions. For ^{242}Am we find good agreement, however, there are significant differences at the fission thresholds of ^{243}Cm and ^{244}Cm and above 7.5 MeV for ^{244}Cm. The uncertainties of our data are generally much lower than the ones of previous measurements by Gavron et al. [9] and Back et al. [7, 24, 25]. Therefore, our data can be used to provide additional constraints on the barrier parameters and level densities of the nuclei investigated. We have observed clear sub-threshold structures for ^{243}Cm. It would be desirable to perform dedicated experiments to investigate these structures with sufficient statistics, at different detection angles of the ejectile and in combination with measurements of the fission-fragment angular distributions.

We have extracted information on the properties of the fission barriers and the level-density parameters of the investigated nuclei by comparing our results to statistical-model calculations. Our model is based on the simple assumption of a double-humped barrier in the complete damping limit. We have determined the uncertainties of the parameters in a rigorous way. These uncertainties show that our data provide a significant constrain on the parameters of the first barrier of ^{243}Cm, ^{242}Am and ^{241}Am, which have been determined with an uncertainty of less than 200 keV. The other barrier parameters of ^{243}Cm, ^{242}Am and ^{241}Am, and the ensemble of barrier parameters of ^{244}Cm and are affected by larger uncertainties. Our results are in general good agreement with the barrier parameters reported in literature. The experimental data are well reproduced using asymptotic level-density parameters at the barriers $\tilde{a}_x$ that agree within rather large error bars with the values recommended in RIPL3 [33].

Acknowledgements

We thank I. Ahmad, J.P. Greene, and R.V.F. Janssens from the Argonne National Laboratory for the production of the ^{243}Am targets. The authors are also indebted to the tandem accelerator staff and the target laboratory of the IPN Orsay for their support during the experiment. We also wish to thank E. Bauge for performing the optical-model calculation. This work was supported by the French national research program GEDEPEON and the Conseil Régional d'Aquitaine.

References

[1] J. A. Northrop, R. H. Stokes and K. Boyer, Phys. Rev. 115 (1959) 1277.
[2] H. C. Britt and J. D. Cramer, Phys. Rev. 181 (1969) 1634.
[3] A. Gavron, H. C. Britt, E. Konecny, J. Weber and J. B. Wilhelmy, Phys. Rev. Lett. 34 (1975) 827.
[4] J. Van Der Plicht, M. N. Harakeh, A.V. D. Woude, P. David, J. Debrus, H. Janszen and J. Schulze, Nucl. Phys. A 346 (1980) 349.
[5] J. R. Wu, J. R. Beene, C. E. Bemis, F. E. Bertrand, E. E. Gross, D. J. Horen and W. P. Jones, Phys. Rev. C 24 (1981) 500.
[6] A. K. Sinha, P. David, H. Hanscheid, F. Risse, C. Rosel and W. Schrieder, J. Phys. G 18 (1992) L105.
[7] B. B. Back, O. Hansen, H. C. Britt and J. D. Garrett, Phys. Rev. C 9 (1974) 1924.

[8] P. D. Goldstone, F. Hopkins, R. E. Malmin and P. Paul, Phys. Rev. C 18 (1987)1706.
[9] A. Gavron et al., Phys. Rev. C 13 (1976) 2374.
[10] S. E. Larsson, I. Ragnarsson and S. G. Nilsson, Phys. Lett. B 38 (1972) 269.
[11] H. C. Britt, W. R. Gibbs, J. J. Griffin and R. H. Stokes, Phys. Rev. 139 (1965) B354.
[12] H. C. Britt and F. Plasil, Phys. Rev. 144 (1966) 1046.
[13] H. C. Britt, F. A. Rickey and W. S. Hall, Phys. Rev. 175 (1968) 1525.
[14] J. D. Cramer and H. C. Britt, Phys. Rev. C 2 (1970) 2350.
[15] H. C. Britt and D. J. Cramer, Phys. Rev. C 2 (1970) 1758.
[16] J. D. Cramer and H. C. Britt, Nucl. Sci. Eng. 41 (1970) 177.
[17] J. E. Escher et al., Rev. Mod. Phys. 84 (2012) 353.
[18] G. Kessedjian et al., Phys. Lett. B 692 (2010) 297.
[19] C. Rodriguez-Tajes et al., Phys. Rev. C 89 (2014) 024614.
[20] G. F. Knoll, Radiation, detection and measurement, third edition (2000) John Wiley & sons, Inc.
[21] T. Kawano et al., Nucl. Data Sheets 109 (2008) 2817.
[22] G. Kessedjian, Ph.D thesis, Université de Bordeaux, France (2008). http://ori-oai.u-bordeaux1.fr/pdf/2008/KESSEDJIAN_GREGOIRE_2008.pdf
[23] D.L Smith, Probability, statistics, and data uncertainties in nuclear science and technology, vol.4, OECD, 1991.
[24] B. B. Back, J. P. Bondorf, G. A. Otroschenko, J. Pedersen and B. Rasmussen, Nucl. Phys. A 165 (1971) 449.
[25] B. B. Back, H. C. Britt, O. Hansen, B. Leroux and J. D. Garrett., Phys. Rev. C 10 (1974) 1948.
[26] P.E. Vorotnikov et al., Yadern. Fiz. 40 (1984) 1141.
[27] E. Bauge, J.P. Delaroche and M. Girod, Phys. Rev. C 63 (2001) 024607.
[28] E. Bauge et al., Phys. Rev. C 61 (2000) 034306.
[29] J.F. Berger, M. Girod and D. Gogny, Comput. Phys. Commun. 63 (1991) 365.
[30] M. J. Martin, Nucl. Data Sheets 106 (2005) 89.
[31] Y. A. Akovali, Nucl. Data Sheets 96 (2002) 177.
[32] Y. A. Akovali, Nucl. Data Sheets 103 (2004) 515.
[33] R. Capote et al., Nucl. Data Sheets 110 (2009) 3107.
[34] J. Kopecky and M. Uhl, Phys. Rev. C 41 (1990) 1941.
[35] A. V. Ignatyuk, J. L. Weil, S. Raman and S. Kahane, Phys. Rev. C 47 (1993) 1504.
[36] A. Bohr and B.R. Mottelson, Nuclear Structure Vol. II, World Scientific, Singapore, 1998.
[37] W.M. Howard and P. Möller, At. Data Nucl. Data Tables 25 (1980) 219.
[38] S. Bjornholm, A. Bohr and B. R. Mottelson, Proceedings of the AIEA Symposium on "Physics and Chemistry of Fission" Vol. I, Rochester New York, 13-17 August 1973, p. 367.
[39] M. B. Lewis, Phys. Rev. C 11 (1975) 145.
[40] B. L. Andersen, B. B. Back and J. M. Bang, Nucl. Phys. A 147 (1970) 33.
[41] I. Thompson and J. Escher, Technical Report UCRL-TR-225984, Lawrence Livermore National Laboratory, 2006.

[42] S. Bjørnholm and J.E. Lynn, Rev. Mod. Phys. 52 (1980) 725.
[43] Y. Avni, The Astrophysical Journal 210 (1976) 642